

# Multi-instrument view on solar eruptive events observed with the Siberian Radioheliograph: From detection of small jets up to development of a shock wave and CME

V.V. Grechnev, S.V. Lesovoi, A.A. Kochanov, A.M. Uralov, A.T. Altyntsev, A.V. Gubin, D.A. Zhdanov, E.F. Ivanov, G.Ya. Smolkov, L.K. Kashapova

*Institute of Solar-Terrestrial Physics, Irkutsk, Russia*

---

## Abstract

The first 48-antenna stage of the Siberian Radioheliograph (SRH) started single-frequency test observations early in 2016, and since August 2016 it routinely observes the Sun at several frequencies in the 4–8 GHz range with an angular resolution of 1–2 arc minutes and an imaging interval of about 12 seconds. With limited opportunities of the incomplete antenna configuration, a high sensitivity of about 100 Jy allows the SRH to contribute to the studies of eruptive phenomena along three lines. First, some eruptions are directly visible in SRH images. Second, some small eruptions are detectable even without a detailed imaging information from microwave depressions caused by screening the background emission by cool erupted plasma. Third, SRH observations reveal new aspects of some events to be studied with different instruments. We focus on an eruptive C2.2 flare on 16 March 2016 around 06:40, one of the first flares observed by the SRH. Proceeding from SRH observations, we analyze this event using extreme-ultraviolet, hard X-ray, white-light, and metric radio data. An eruptive prominence expanded, brightened, and twisted, which indicates a time-extended process of the flux-rope formation together with the development of a large coronal mass ejection (CME). The observations rule out a passive role of the prominence in the CME formation. The abrupt prominence eruption impulsively excited a blast-wave-like shock, which appeared during the microwave burst and was manifested in an “EUV wave” and Type II radio burst. The shock wave decayed and did not transform into a bow shock because of the low speed of the CME. Nevertheless, this event produced a clear proton enhancement near Earth. Comparison with our previous studies of several events confirms that the impulsive-piston shock-excitation scenario is typical of various events.

*Keywords:* Coronal Mass Ejections, Instrumentation and Data Management, Prominences, Radio Bursts, Surges, Shock Waves

---

## 1. Introduction

Solar flares, coronal mass ejections (CMEs), associated shock waves, and related phenomena are known as causes of space weather disturbances. Hard electromagnetic emissions and energetic particles pose hazard to space-borne equipment, astronauts on spacecraft, and even crew members and passengers on aircraft that carry out transocean flights entering high latitudes. CME-associated shock waves travel over large distances in the heliosphere, being responsible for the geomagnetic storm sudden commencement (SSC). Magnetic structures of CMEs hitting the Earth’s magnetosphere can cause strong geomagnetic storms.

In spite of a certain space weather impact, the origin and interrelation of solar eruptive phenomena are still not quite clear. Comprehending solar eruptions is hampered by observational difficulties. The existing concepts are mostly based on the hypotheses that were proposed several decades ago and back-extrapolated results of in-situ measurements in near-Earth space.

According to a widely accepted view, the main driver of a solar eruption is a magnetic flux rope. It is considered as the active structure of a CME that governs its development

and subsequent expansion. The flux rope is traditionally assumed to be associated with the CME cavity. Prominences (filaments) or associated structures appear to be among the most probable flux-rope progenitors (Gibson, 2015). However, genesis of flux ropes, their size range, and other properties are not clear so far. According to some concepts, the flux rope pre-exists before the eruption onset (Chen, 1989, 1996; Cheng et al., 2013). Different concepts relate the flux-rope formation to reconnection processes, which are also responsible for solar flares (Inhester et al., 1992; Longcope and Beveridge, 2007; Qiu et al., 2007).

There is no consensus about coronal shock waves. Some authors advocate flare-ignited blast waves at least in some events (Magdalenic et al., 2010, 2012; Nindos et al., 2011). Different studies demonstrate the CME-related origin of shock waves to be more probable (e.g. Cliver et al., 2004). While basic excitation mechanisms of shock waves seem to be known (see, e.g., Vršnak and Cliver, 2008), observational difficulties result in large uncertainties in their identification.

Solar eruptions and associated phenomena are manifested in different spectral domains, including microwaves. Radio emission is produced by various mechanisms, providing im-

portant information on these phenomena and responsible processes. Being sensitive to gyrosynchrotron emission of non-thermal electrons, microwaves reveal the flare regions. The microwave spectrum contains information about accelerated electrons and magnetic fields in the corona. Being sensitive to thermal plasma emission, microwave images show eruptive prominences (filaments). Screening background solar emission by erupted prominence material sometimes produces depressions detectable even in the total microwave flux (Covington and Dodson, 1953) termed the “negative bursts”. From studies of the negative bursts, events with reconnection between erupting structures and a large-scale coronal magnetic environment were identified (Grechnev et al., 2013b, 2014b; Uralov et al., 2014). These examples demonstrate significant contribution to studies of solar eruptions from microwave imaging and non-imaging observations.

Microwave images produced by radio heliographs generally have a poorer spatial resolution relative to extreme-ultraviolet (EUV) and X-ray telescopes. Nevertheless, sometimes it is even possible to judge about the structures that are unresolved in microwave images (Grechnev and Kochanov, 2016; Grechnev et al., 2017a; Lesovoi et al., 2017).

In 2016, the first 48-antenna stage of the Siberian Radioheliograph (SRH; Lesovoi et al., 2014, 2017) started observing the Sun. An overview of the SRH data has revealed several indications of eruptions. Proceeding from these indications, we consider a few eruptive events observed by different instruments and endeavor to address the challenges listed in this section. We pay special attention to the 16 March 2016 eruptive event, one of the first flares observed by the SRH (Lesovoi et al., 2017). Multi-instrument analysis of large-scale aspects of this event promises shedding additional light on the development of a CME and associated shock wave.

Section 2 outlines the SRH. Section 3 presents observations of microwave depressions caused by small jets. Section 4 presents direct observations of a spray on 1 May 2017. Section 5 is devoted to a multi-instrument analysis of an eruptive event on 16 March 2016 that produced a CME and caused a near-Earth proton enhancement. Section 6 discusses the results and shows their relevance to a typical eruptive event. Section 7 summarizes our conclusions and their implications and presents last changes in the functionality of the SRH.

## 2. SRH: 48-Antenna First Stage

The SRH was constructed as an upgrade of the Siberian Solar Radio Telescope (SSRT; Smolkov et al., 1986; Grechnev et al., 2003). The SSRT was designed as a cross-shaped interferometer comprising two linear arrays in the EW and SN directions, each with 128 equidistant antennas of 2.5 m diameter spaced by  $d = 4.9$  m. The SSRT scans the Sun due to its diurnal passage through the fan beam formed by the simultaneous receiving at a number of different but close frequencies in the 5.67–5.79 GHz band. Thus, the SSRT can produce the images practically at a single frequency every 2–3 minutes at most.

Unlike the directly-imaging SSRT, the SRH uses the Fourier synthesis. The temporal resolution determined by the receiver

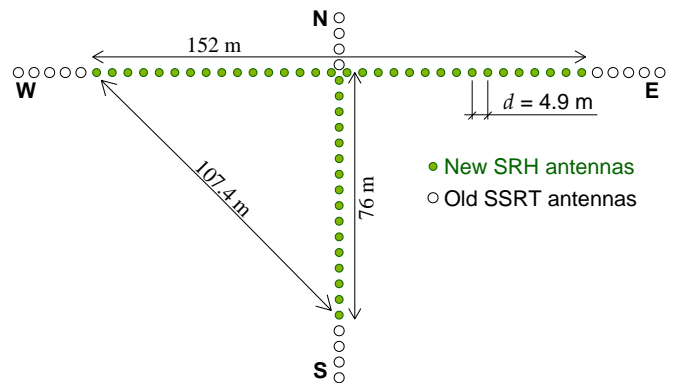


Figure 1: The T-shaped configuration of the 48-antenna SRH first stage. The remote parts of the four SSRT arms (each arm of 311 m) with remaining old antennas are not shown.

system is much higher than the SSRT had. The SRH has a T-shaped antenna array. Its 1.8 m antenna elements replace old SSRT antennas, being installed at the existing posts along the east, west, and south arms. The first 48-antenna stage constitutes a dense equidistant part of a future complete SRH antenna array (Figures 1 and 2). Being redundant, this array provides a high sensitivity, which is about 1000 K in the images and reaches for compact sources  $10^{-4}$  of the total solar flux, i.e. about 100 Jy (Lesovoi and Kobets, 2017).

Both circularly-polarized components are measured. The observing frequencies, each of the 10 MHz bandwidth in the 4–8 GHz range, are set by software and can be optimized for an observing program. The accumulation time at each frequency is 0.28 s for each circularly-polarized component, and the time to switch from one frequency to another was about 2 s in 2016 and 2017. The maximum baseline used is 107.4 m, enabling a spatial resolution down to  $70''$  at 8 GHz.

The SRH systems outlined in Figure 3 were mostly developed and constructed by the SRH team. The top image represents a single antenna element. The antenna feed receives two orthogonal linearly-polarized signals, which come into the frontend unit. A 3-dB  $90^\circ$  hybrid coupler performs the linear-to-circular polarization conversion of the input signals. Then they are pre-amplified and come to a switch, which alternately passes the left-handedly polarized signal (LCP) and the right-handedly polarized one (RCP). The signals from the output of the switch come through the second amplifier to a diode laser, which converts the ultrahigh-frequency (UHF) signals to optical signals for their transmission to the working building. The total gain of the frontend unit is 30–40 dB.

The signal from each antenna element is transmitted to the backend of the receiver located in the working building (Figure 2) through the optical fiber link located in the tunnel. Each backend unit (Figure 3, bottom-left) processes the signals from four antennas. The input optical signals are converted back to the UHF, amplified, transformed to an intermediate frequency, and digitized at 100 MHz. Their subsequent digital processing includes the formation of the operating frequency band, coarse and fine compensation for the geometric delays and difference in the cable lengths, and fringe stopping. Finally the digital sig-



Figure 2: View of the 48-antenna SRH first stage (the east arm). White remote larger dishes on the right (east) belong to the old SSRT antenna system. Separate dishes on the ground behind the SRH antennas belong to the total-flux spectropolarimeters (Zhdanov and Zandanov, 2015). The receiver and control systems are located in the working building visible behind the SRH antennas on the left.

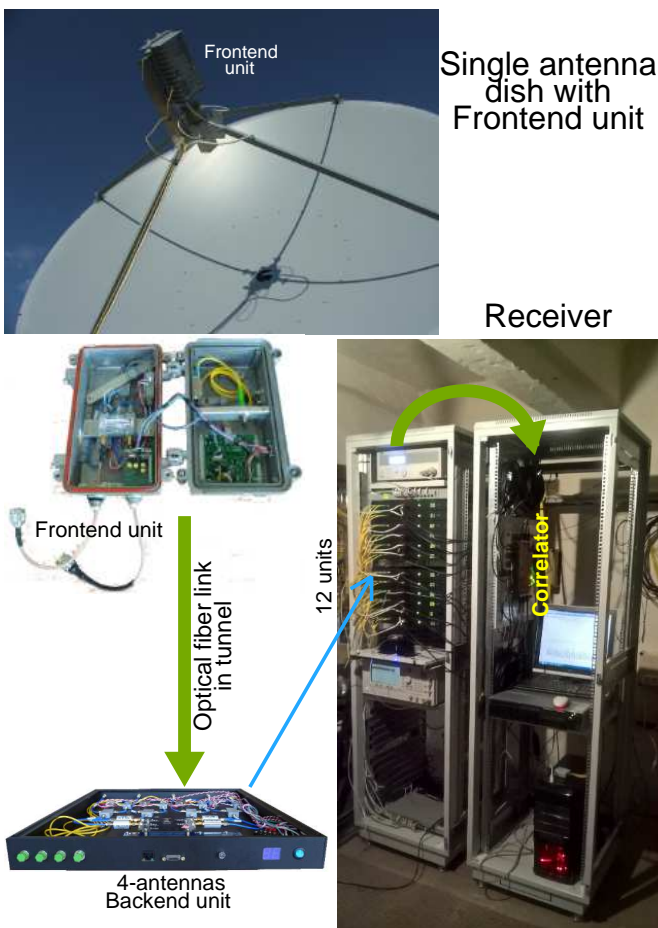


Figure 3: A scheme of the SRH hardware. The frontend units (middle left) are installed in all antenna elements (top left). The backend of the receiver and the correlator (bottom right) are located in the working building. Twelve backend units are mounted in the left cabinet, and the correlator is located in the right cabinet. The green arrows denote the paths of the signals.

nals come to a correlator mounted in the right cabinet shown in Figure 3 (bottom right). The correlator currently produces 512 complex visibilities for the imaging and several tens of those for the calibration purposes. Redundant baselines are not used in the imaging.

Single-frequency test observations started at the SRH early in 2016. Since July 2016 till December 2017, the SRH routinely observed the Sun at five frequencies. To monitor solar activity and main SRH systems, the so-called correlation plots are used. Being a proxy of radio flux, they represent temporal variations in the sum of cross-correlations of all antenna pairs (Lesovoi and Kobets, 2017) and show the changes in both the brightness and structure of the sources. Real-time correlation plots and quick-look images produced by the SRH at a set of the operating frequencies are accessible online at the SRH Web site <http://badary.iszf.irk.ru/>. Adjustment of the SRH systems is still in progress.

Raw SRH data contain complex visibilities measured at a given set of frequencies in right and left circularly-polarized components, information on the array geometry, time stamps, etc. The data are stored in binary FITS tables. The Python-based library providing basic programming user interfaces for data handling, phase calibration, and interferometric imaging routines is under development.

The phase calibration tasks use the baseline redundancy of the east, west, and south SRH arms and resolve phase ambiguities in a sense of an overdetermined optimization problem. To clean raw SRH images, we tentatively apply an MS-CLEAN algorithm (Cornwell, 2008). Parameters of the algorithm would be adjusted to meet diverse observational requirements.

The technique to calibrate the images in brightness temperatures (Kochanov et al., 2013; Lesovoi et al., 2017) is based on a well-known method by referring to the most frequent pixel values over the solar disk and those over the sky. We refer the quiet-Sun brightness temperature to the measurements

by Zirin et al. (1991) and Borovik (1994), fitting their frequency dependence with a fourth-order polynomial in the log-log scale. In particular, we adopt the values of 21.6, 18.1, 16.0, 14.6, and 13.6 thousand Kelvin at frequencies of 4.0, 5.0, 6.0, 7.0, and 8.0 GHz, respectively.

The remaining outer SSRT antennas of the three arms and the whole north arm continue observing in the original operating mode, providing the images of compact sources at 5.7 GHz with a resolution of down to 21". Daily quick-look SSRT images near the local noon are available at the SRH Web site.

### 3. Microwave Depressions

Temporary depressions of the total microwave flux below the quasi-stationary level known as negative bursts were discovered by Covington and Dodson (1953) from observations at 10.7 cm (2.8 GHz). Typically, a negative burst follows an ordinary flare-related impulsive burst, when the eruption screens a radio source located in the same or a nearby active region. The cause of a negative burst is screening by low-temperature absorbing erupted material of a compact microwave source (Covington, 1973; Sawyer, 1977; Maksimov and Nefed'ev, 1991) or/and large areas of the quiet Sun. Hence, microwave depressions indicate probable eruptions. The dependence of the absorption depth on both the observing frequency and properties of absorbing plasma provides a basic possibility to estimate some parameters of an erupting structure, if a depression is observed at different frequencies (see, e.g., Grechnev et al., 2008, 2013b; Kuzmenko and Grechnev, 2017).

Because both the opacity of a filament or surge and its contrast against the solar disk depend on the frequency inversely, the negative bursts are observed mainly at 1–10 GHz. Although eruptions occur often, detection of microwave depressions requires a high sensitivity and calibration stability of total-flux radiometers that makes the negative bursts rare phenomena. From 1990 through 2009, their total number recorded by all ground-based stations was 72 with a maximum yearly number being as small as 14 in 1991 (Grechnev et al., 2013b). Previously negative bursts were observed almost exclusively in total intensity.

With an operating frequency range within 4–8 GHz and a high sensitivity, the SRH observations promise the detection of eruption-related absorption phenomena. A simplest way to detect a microwave depression is provided by the correlation plots. Lesovoi et al. (2017) presented an unprecedented series of three negative bursts observed in one day on 9 August 2016 by the SRH and Nobeyama Radio Polarimeters (NoRP: Torii et al., 1979; Nakajima et al., 1985) in both intensity and polarization. These negative bursts were caused by repeating surges, which screened a polarized sunspot-associated microwave source in active region (AR) 12574 located not far from the limb (N04E59).

Here we present examples of microwave depressions revealed from the SRH data that really point at small eruptions. Some of the eruptions indicated by the SRH are too weak and small to be easily detected from observations at different wavelengths. The possibilities of plasma diagnostics for such eruptions based on the SRH data are discussed in Section 6.1.

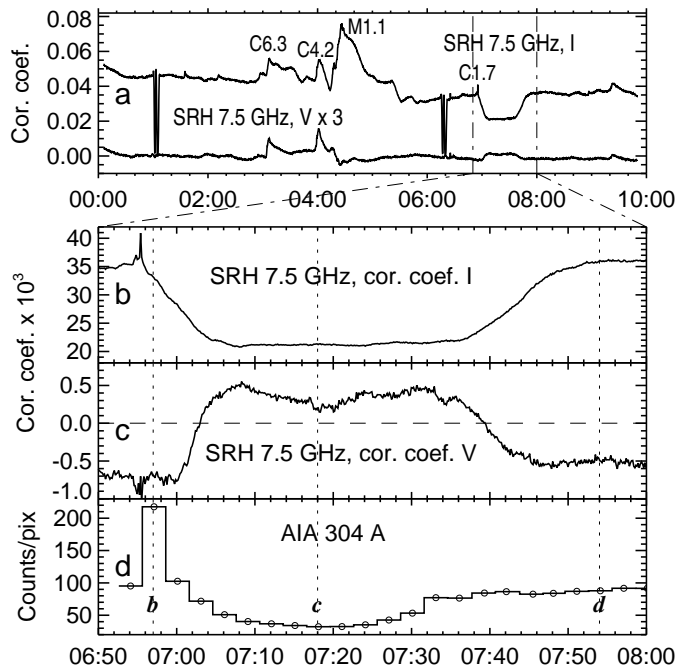


Figure 4: Temporal profiles of the small eruption on 9 September 2017. The temporal profile in panel d was computed over the framed region in Figure 5 from the quarter-resolution beacon AIA 304 Å images with a 3-minute interval. The vertical dotted lines denote the times of the images in Figure 5 whose panels are indicated by the bold-italic letters in panel d.

#### 3.1. A Small Eruption on 9 September 2017

A conspicuous microwave depression recorded on 9 September 2017 is visible between the vertical dash-dotted lines in Figure 4a, which presents the SRH intensity and polarization correlation plots at a frequency of 7.5 GHz. The bursts at 03:06, 04:00, 04:26, and a spiky burst at 06:55 are associated with GOES C6.3, C4.2, M1.1, and C1.7 flares, respectively, all of which occurred in AR 12673. The excursions around 01:00 and 06:15 are caused by the Sun-to-sky calibration maneuvers of the antenna system. The depression in intensity has a counterpart in polarization, indicating the screening of a polarized source. The plots at the other frequencies are similar. The SRH images reveal that the brightness decreased in a microwave source located close to the west limb.

The depression was caused by a small eruption associated with a short (7 minutes) impulsive C1.7/1F flare (S10W70) in AR 12673. This superactive region produced from 4 through 10 September four X-class flares and numerous weaker events. The major eruptive events in this region caused strong fluxes of energetic particles, a severe geomagnetic storm on 7–9 September, a deep Forbush decrease, and a ground-level enhancement of cosmic-ray intensity (GLE73) on 10 September, as AR 12673 arrived at the west limb. The event of interest was much weaker.

The intensitygram in Figure 5a produced on 9 September by the *Helioseismic and Magnetic Imager* (HMI: Scherrer et al., 2012) onboard the *Solar Dynamics Observatory* (SDO) shows that AR 12673 comprised several sunspots. It had a complex magnetic  $\beta\gamma\delta$ -configuration. Figures 5b–5d present three

episodes of the small event observed by the *Atmospheric Imaging Assembly* (AIA; Lemen et al., 2012) onboard SDO in the 304 Å channel, which is most sensitive to low-temperature plasma. Here we used quarter-resolution beacon AIA files available with an interval of 3 minutes. AIA did not observe the whole Sun between 06:27 and 06:54. Figure 5b shows a flare brightening with a circular ribbon. Figure 5c reveals a jet-like eruption. Figure 5d presents the active region after the event.

Figures 4b and 4c show expanded correlation plots in intensity and polarization. While the structure of the active region is unresolved by the SRH, the change in the polarization indicates the screening of one or more sunspot-associated sources in AR 12673. Figure 4d presents the average brightness in 304 Å over the framed region in Figure 5 to compare the EUV and microwave observations. The microwave depression lasted somewhat longer than the jet was visible in the 304 Å images.

The 2017-09-09\_AIA304\_WL\_SRH.mpg movie presents the course of the event as observed by AIA in 304 Å (left) in comparison with HMI intensitygrams (right). The bottom plot shows the same 304 Å light curve in Figure 4d in white and the 7.5 GHz correlation plots in yellow scaled to match the plotted range. The red vertical line on the plots marks the current observation time. A short-lived flare brightening visible in one image is followed by an eruption (surge) from the same region. The rising material of the surge is initially narrow and bright that indicates its temperature of order  $5 \times 10^4$  K. Then the surge broadens, darkens, and screens the structures behind it. The absorption indicates a temperature of the erupted material of  $< 10^4$  K. The surge partly covers a sunspot group in AR 12673 behind it. The screening of microwave sources above the sunspots causes the depression in total intensity and change in polarization. After 07:20 the opacity of the surge gradually decreases that corresponds to the recovery of the 304 Å emission flux. The microwave emission recovers later.

The depression was preceded by a small microwave burst around 06:55 corresponding to the flare brightening. Simultaneously, a group of metric Type III bursts was observed from 06:53 to 06:56 extending down to the kilometric range that indicates escape of accelerated electrons into the interplanetary space. No CME followed this event.

### 3.2. A Microeruption on 3 August 2017

A microwave depression caused by a still weaker eruptive event was observed on 3 August 2017. Figures 6 and 7 present the event occurring in AR 12670 (S06 E55) in the formats similar to those in the preceding section. Note that the SRH correlation coefficients here were one order of magnitude smaller than in the 9 September 2017 event. To reduce the noise, they were smoothed in Figures 6b and 6c with a 15-samples-wide boxcar.

The circumstances of the 3 August and 9 September events are mainly similar. A brightening visible in 304 Å near a single isolated sunspot located not far from the east limb was followed by a tiny surge (the arrow in Figure 7c) that overlapped with a sunspot-associated polarized microwave source and partly screened its emission.

However, the spatial size and energy of this event were considerably smaller. The field of view in Figure 7 roughly corre-

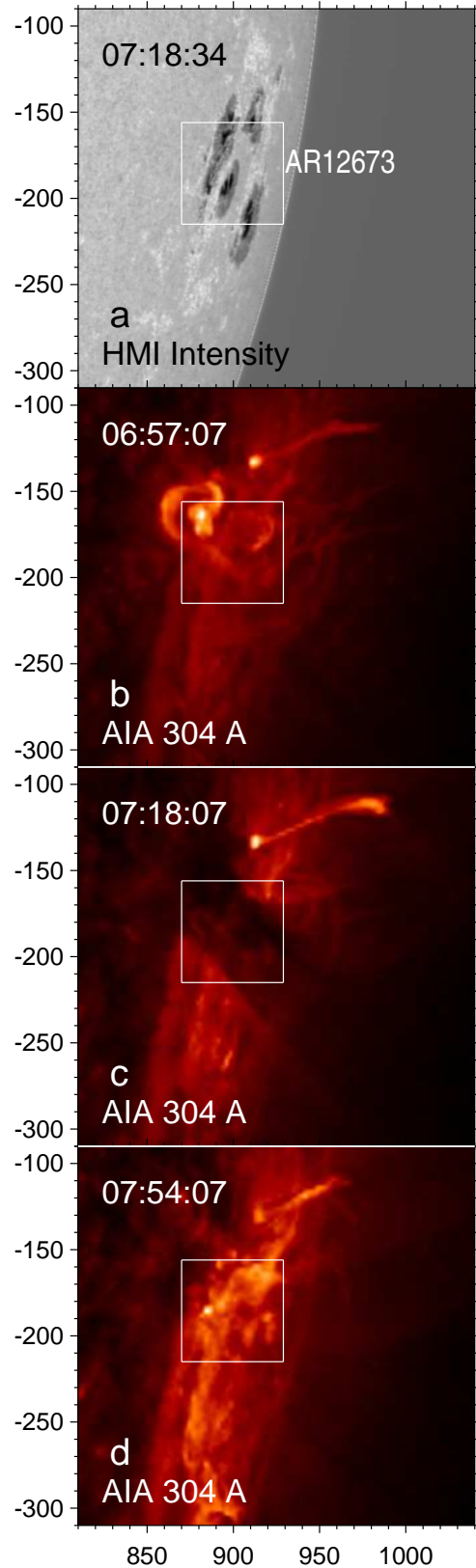


Figure 5: Small eruption on 9 September 2017 in the SDO/AIA 304 Å images (b–d) in comparison with a sunspot group visible in an HMI intensitygram (a). The axes indicate the distance from solar disk center in arcseconds.

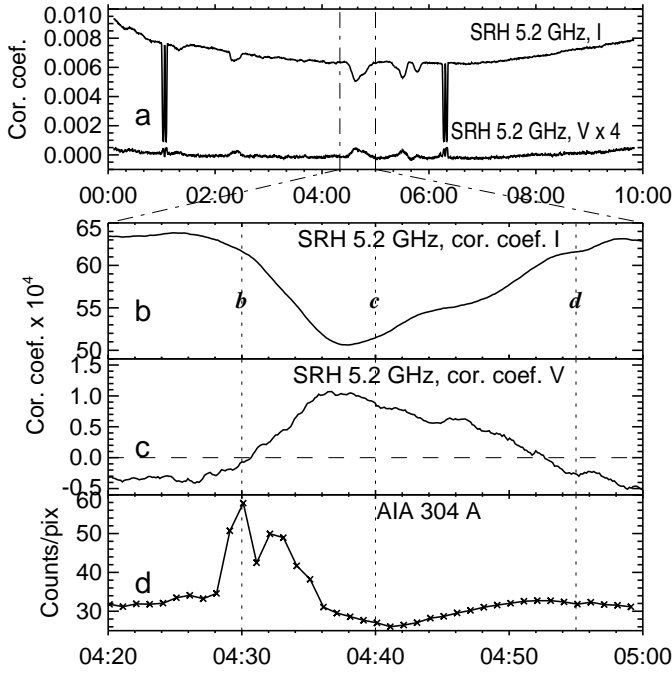


Figure 6: Time profiles of the microeruption on 3 August 2017. The time profile in panel d was computed over the framed region in Figure 7 from full-resolution AIA 304 Å images taken with a 1-minute interval. The vertical dotted lines denote the times of the images in Figure 7 whose panels are indicated by the bold-italic letters in panel b.

sponds to the SRH beam size, while the region of brightening is poorly visible even in the full-resolution AIA 304 Å images. There were no Type III bursts and no CME. No response to this event is present in X-rays, and its detection in AIA images is not a simple task. Nevertheless, this microeruption is clearly visible in the SRH correlation plots, while its location is easily identified from the SRH images.

The correlation plots in Figure 6a reveal more depressions on that day. At least one of them, around 02:20, was caused by a similar microeruption in the same active region. Depressions are also detectable in the SRH data on some different days.

#### 4. A Spray Observed on 1 May 2017

The eruptive event on 1 May 2017 associated with a B9.9 flare in active region 12652 (N18W78) was directly observed by the SRH. Figure 8 presents the images of the event produced by the SRH at 5.2 GHz in the left column along with temporally close SDO/AIA 304 Å images in the right column. Note that the solar disk is subtracted in the SRH images (the quiet-Sun brightness temperature at 5.2 GHz is 17570 K) and reduced in the 304 Å images of this event to emphasize the off-limb spray. The flare region is denoted by the solid contour in Figures 8b and 8c. The eruption is outlined in Figures 8c–8e by the thick gray-dashed circle.

Figures 8a and 8f show the situation before the event. A compact flare brightening appears in Figures 8b and 8g. A spray appears in the next row (Figures 8c, h); the SRH shows its thickest part with a considerably poorer resolution relative to SDO/AIA.

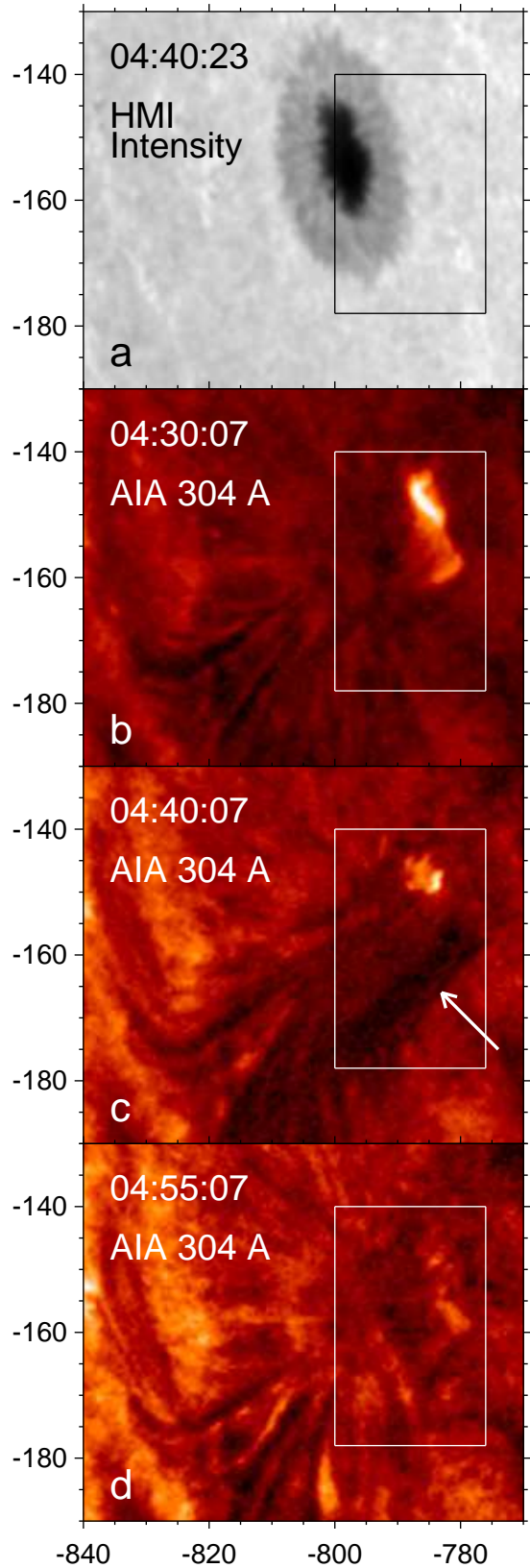


Figure 7: Microeruption on 3 August 2017 in the SDO/AIA 304 Å images (b–d) in comparison with a sunspot visible in an HMI intensitygram (a). The arrow in panel c indicates a tiny surge. The axes indicate the distance from solar disk center in arcseconds.

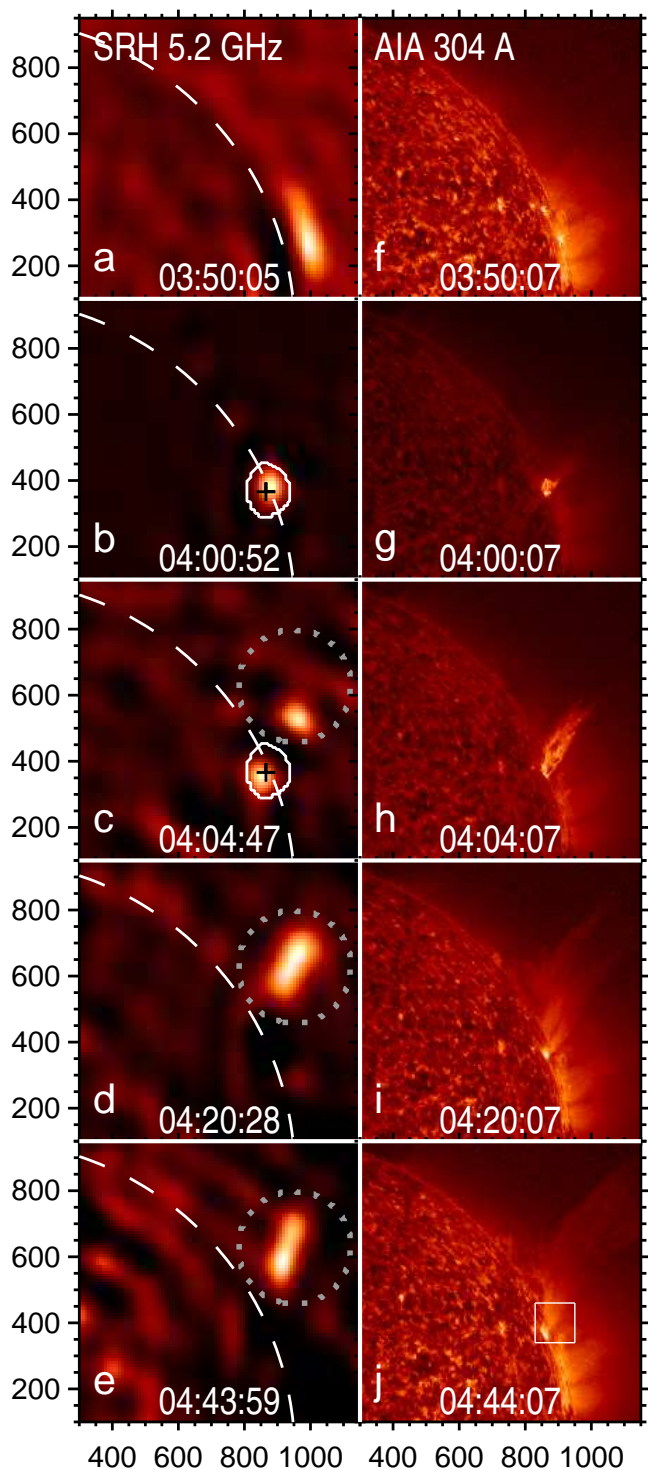


Figure 8: Eruption on 1 May 2017 in dirty SRH 5.2 GHz images (a–e) in comparison with SDO/AIA 304 Å images (f–j). The solar disk is subtracted in the SRH images and reduced in the AIA images. The dashed arc denotes the limb. The solid contours in panels b, c outline the flaring source. The gray-dashed circle in panels c–e outline the off-limb eruption. The temporal profiles over the contoured region are presented in Figure 9a. The black cross in panels b, c denote the center of the X-ray source in RHESSI images. The frame in panel j denotes the field of view in Figure 10. The axes indicate the distance from solar disk center in arcseconds.

Then, the flaring source disappears at 5.2 GHz, while a portion of the off-limb spray is still present in the SRH images. The spray broadens in 304 Å; a part of its material returns to the solar surface.

The black cross in Figures 8b, c denotes the brightness center of an X-ray source observed by the *Reuven Ramaty High-Energy Solar Spectroscopic Imager* (RHESSI; Lin et al., 2002). The centers of the source observed at 3–6 keV, 6–12 keV, and 12–25 keV coincide to within 2.5". A response is detectable in the RHESSI count rate up to the 25–50 keV band.

Figure 9a presents the temporal profiles computed from the SRH images (synthesized with a one-minute interval) over the contoured regions in comparison with a GOES 1–8 Å flux shown in Figure 9b in the linear scale. The similarity of the microwave burst (black) with a soft X-ray (SXR) flux suggests domination of the microwaves by thermal emission, consistent with a flatness within  $\pm 8\%$  of the flux spectrum measured from the SRH images at 4.0–6.8 GHz. The thermal bremsstrahlung estimated from GOES data provides 0.8 sfu equal to the microwave flux actually observed. The same flux of the microwave source was computed from the 17 GHz image produced by the Nobeyama Radioheliograph (NoRH; Nakajima et al., 1994) at 04:00. This weak microwave burst is not detectable in NoRP or Learmonth data. It is only shown by the RT-2 radio telescope of the Ussuriysk Astrophysical Observatory (Kuz'menko et al., 2008) at 2.8 GHz, where its flux was also about 0.8 sfu. A flat microwave spectrum over a six-fold frequency range confirms that the burst was due to optically thin free-free emission.

Unlike the SXR burst followed by a shoulder, the microwave burst changed to a depression, which lasted one hour (Figure 9). The depression was most likely caused by absorption of the microwave emission in the low-temperature plasma of the spray. A dark absorbing material is really visible in the combined 211 Å and 304 Å AIA images in Figure 10d. The similarity between the temporal profile in Figure 9c computed from the 211 Å images over the framed region and the microwave profile of the flare region confirms the absorption-related origin of the microwave depression. The total microwave flux emitted by the off-limb spray is represented by the thick-gray line in Figure 9a. The temporal profile of the microwave depression resembles an inverted profile of the spray that also confirms their common cause.

The filament eruption is seen in combined SDO/AIA 304 Å and 211 Å images in Figure 10, whose field of view is denoted by the frame in Figure 8j. A part of a dark pre-eruptive filament in Figure 10a screens the bright emission above a plage. In Figure 10b, a thick circular structure bound with the filament brightens up. The eruption process strengthens in Figure 10c corresponding to the peak of the microwave and X-ray bursts. Two Type III bursts occurred at that time extending to the kilometric range that suggests the appearance of accelerated electrons and their escape into the interplanetary space. The brightest compact source was located in the southwest part of the configuration. Figure 10d shows outflow of low-temperature plasma along the main legs of the erupting filament. This plasma partly returned back later. The low-temperature plasma

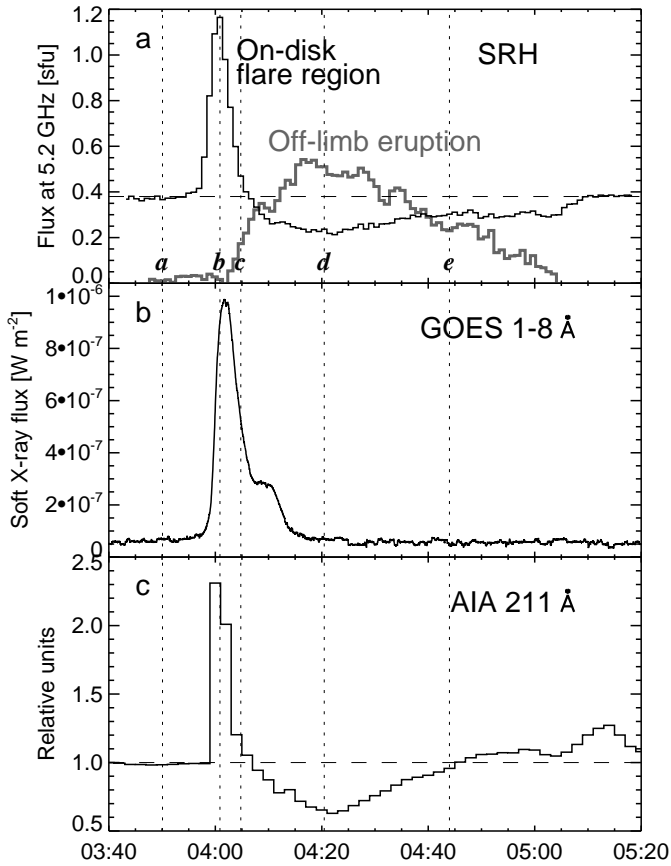


Figure 9: Temporal profiles of the 1 May 2017 eruptive event. a) Microwave flux profiles computed from the SRH images at 5.2 GHz over the flare region (black; solid contour in Figures 8b, c) and over the off-limb spray (gray; dotted contour in Figures 8c–e). The labels at the bottom denote the observation times of the corresponding panels in Figure 8. b) GOES 1–8 Å plot. c) Temporal profile computed from the 211 Å images over a framed region in Figure 10d.

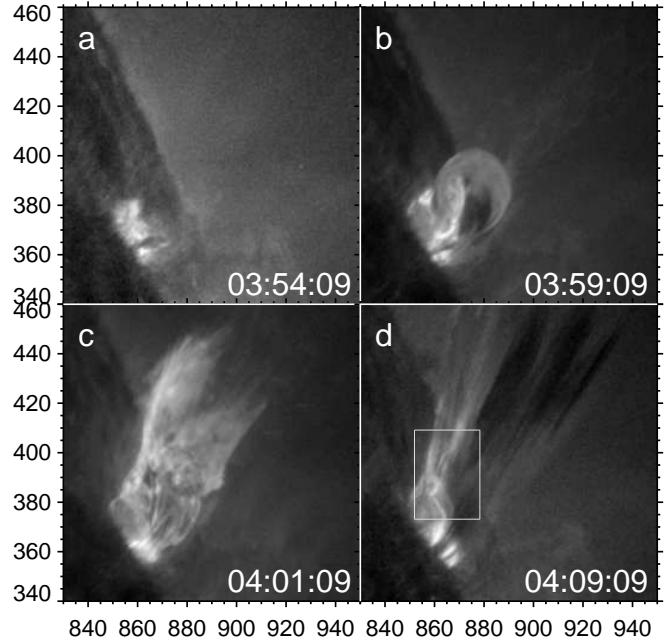


Figure 10: Eruption region on 1 May 2017 in combined SDO/AIA 304 Å and 211 Å images. The times averaged between both images separated by 4.5 s are specified in the panels. The axes indicate the distance from solar disk center in arcseconds.

flow screened the bright microwave-emitting source that caused the depression in the temporal profile in Figure 9a.

A supplementary 2017-05-01\_AIA304\_SRH.mpg movie presents the development of the large-scale spray in 304 Å images (right) and the SRH observations at 5.2 GHz (left). The impulsive flare brightening is maximum at 04:00. A bright erupted material appears at 04:02. A dark absorbing low-temperature material appears at 04:04 which corresponds to the decay of the spike at 5.2 GHz in Figure 9a and in 304 Å in Figure 9c. The rising motion of the dark material is visible until 04:14, and then its returning motion starts. The erupted material visible in 304 Å gradually falls until the end of the movie (corresponding to the end of the depression in Figures 9a, c), while its amount decreases.

Figure 11 shows a mass ejection observed by the *Large Angle Spectroscopic Coronagraph* (LASCO; Brueckner et al., 1995) onboard SOHO. The ejection also looks like a spray and does not exhibit a flux-rope-like magnetic structure. A trailing part of the ejected material (dark in the running differences) indicated by the arrows returned to the surface. The ejection dispersed in solar wind and disappeared in the LASCO-C3 field of view.

## 5. The 16 March 2016 Event Associated with a CME and Shock Wave

Unlike the small eruptions not associated with CMEs presented in Section 3, here we consider an eruptive-flare event, which occurred on 16 March 2016 in AR 12522 (N14 W83) and had a GOES importance of C2.2. The event gave rise to a CME and shock wave and produced a weak near-Earth proton enhancement. This was the first flare observed by the SRH, when

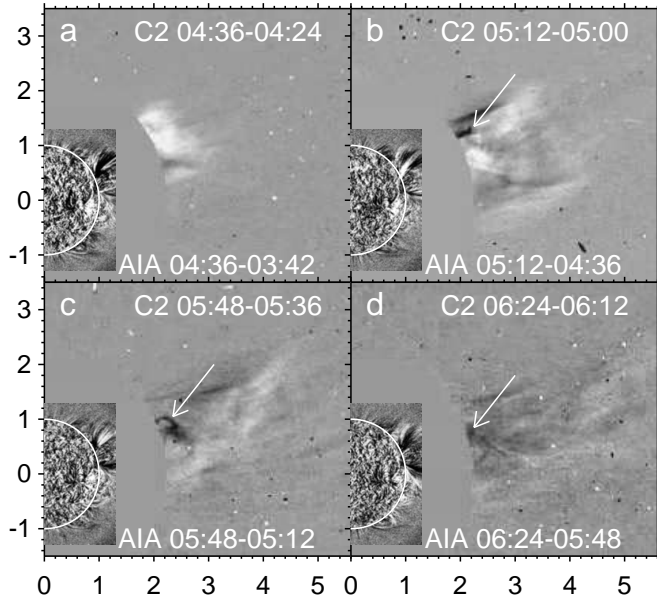


Figure 11: Mass ejection on 1 May 2017 in LASCO-C2 running-difference images. The insets show the AIA 193 Å image ratios. The arrows point at dark features returning to the solar surface. The circles denote the solar limb. The axes indicate the distance from solar disk center in solar radii.

it operated in a single-frequency mode at 6.0 GHz. Here we start from SRH images and follow different stages of the event using imaging and non-imaging observations in hard X-rays, extreme ultraviolet, white-light, and in metric radio range.

### 5.1. SRH Observations and Preliminary Conclusions

We synthesized about 3270 total-intensity (Stokes  $I$ ) images in steps of 1 s for the whole flare duration from 06:35:34 to 07:30:10. Each image was processed separately for the impulsive phase, and we produced 10 s averages for a later stage. Each of the images obtained in this way was calibrated in brightness temperatures individually using the technique described by Kochanov et al. (2013) and referring to the quiet-Sun brightness temperature of 15960 K at 6.0 GHz. All of the images were coaligned. One of the images observed by the SRH before the flare is shown in Figure 12b, and an image observed close to the maximum of the microwave burst is shown in Figure 12d. Nearly simultaneous AIA 193 Å images are shown on the left.

The microwave emission of this flare was too weak to be recorded by total-flux radiometers properly. With an insufficient spatial resolution of the SRH to supply detailed images of the flare site, its sensitivity is high enough to produce a detailed light curve. The total-flux temporal profile was computed from dirty SRH images over the flare region denoted by the dotted white frame in Figures 12b,d. The microwave burst was modest, up to 18 sfu, while a hard X-ray (HXR) burst was considerable.

The impulsive phase of the flare is shown by the 2016-03-16\_SRH\_impulsive\_phase\_inset.mpg movie composed from dirty SRH images with an interval of 1 s. Each full-disk image is displayed with an individual nonlinear

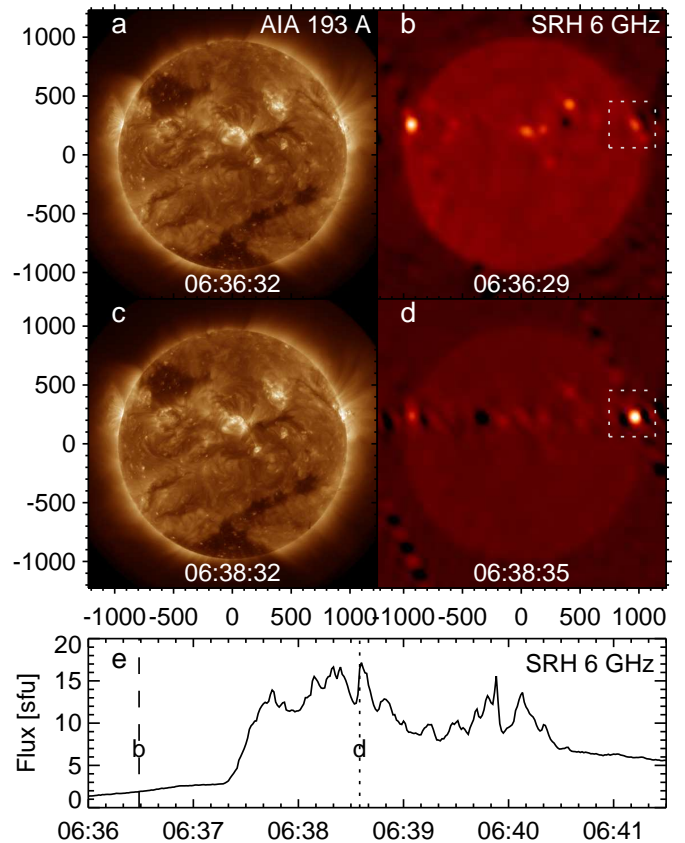


Figure 12: The 16 March 2016 eruptive flare in the AIA 193 Å and clean SRH 6 GHz images: a, b) before the flare, c, d) near the maximum of the microwave burst, e) the total-intensity temporal profile at 6 GHz computed from the SRH images over a framed region in panels (b,d).

brightness scale to reveal the brightness distribution over the solar disk. The top-left inset represents the framed region in a common linear brightness scale over the whole flare. The bottom plot shows the total-flux temporal profile over the framed region with a moving vertical line, which denotes the observation time of the corresponding image.

The 2016-03-16\_AIA193\_304\_SRH\_Fermi.mpg movie presents the prominence eruption observed by AIA in 193 Å (left) and in 304 Å (right) in comparison with the microwave and HXR bursts shown at the bottom. The eruption started first; the bursts became considerable, when intermittent brightenings appeared in 193 Å near the solar surface beneath the rising prominence. The temporal structure of the microwave burst is similar to a temporal profile computed from the running-difference 193 Å images over combined regions of the intermittent brightenings, whereas no similarity was observed with any of the individual regions (Lesovoi et al., 2017).

SRH images indicate an expanding feature above the west limb. At that time, the image of the Sun from an adjacent interference order of the SRH was located close to the main image right on the west, where the erupting prominence expanded. The east–west sidelobes from the flare region and those from a source at the east limb overlapped (Figure 12d), covering the erupting prominence. Unfavorable observation conditions and a low contrast of the erupting prominence determined by a large area of the SRH beam make its analysis from SRH images difficult. We therefore consider EUV observations of the erupting prominence in the next section.

A brief analysis of the flare observed by the SRH and the prominence eruption led Lesovoi et al. (2017) to the following conclusions: 1. Acceleration of most electrons in the flare was initiated by the prominence eruption. 2. Compact microwave sources were located in the legs of the flare arcade throughout its whole length. 3. HXR sources were most likely also distributed over the flare ribbons.

Here we continue with a study of this event, focusing on its large-scale aspects and using data of different instruments. We also pay attention to its space weather impact.

### 5.2. Prominence Eruption

AIA 304 Å images in Figure 13 present some episodes of the prominence eruption. Figure 13a shows the initial static prominence. In Figure 13b, the southern part of the prominence top slightly displaced up, and a gap in its body appeared beneath. Flare ribbons are not yet detectable. In Figure 13c, the prominence considerably stretched up. Its broadest part north of the top brightened up, that indicates heating; note faint cross-shaped diffraction patterns on the photodetector emanating from this bright feature. A flare ribbon appeared. In Figure 13d, the prominence changed still stronger, having acquired a high speed. The top part took a complex shape and started stretching forward. In Figure 13e, the twisted prominence intersected. Two ribbons are visible.

Lesovoi et al. (2017) measured the kinematics of the erupting prominence from AIA 304 Å images. To verify those measurements, we included the 174 Å observations in a wider field

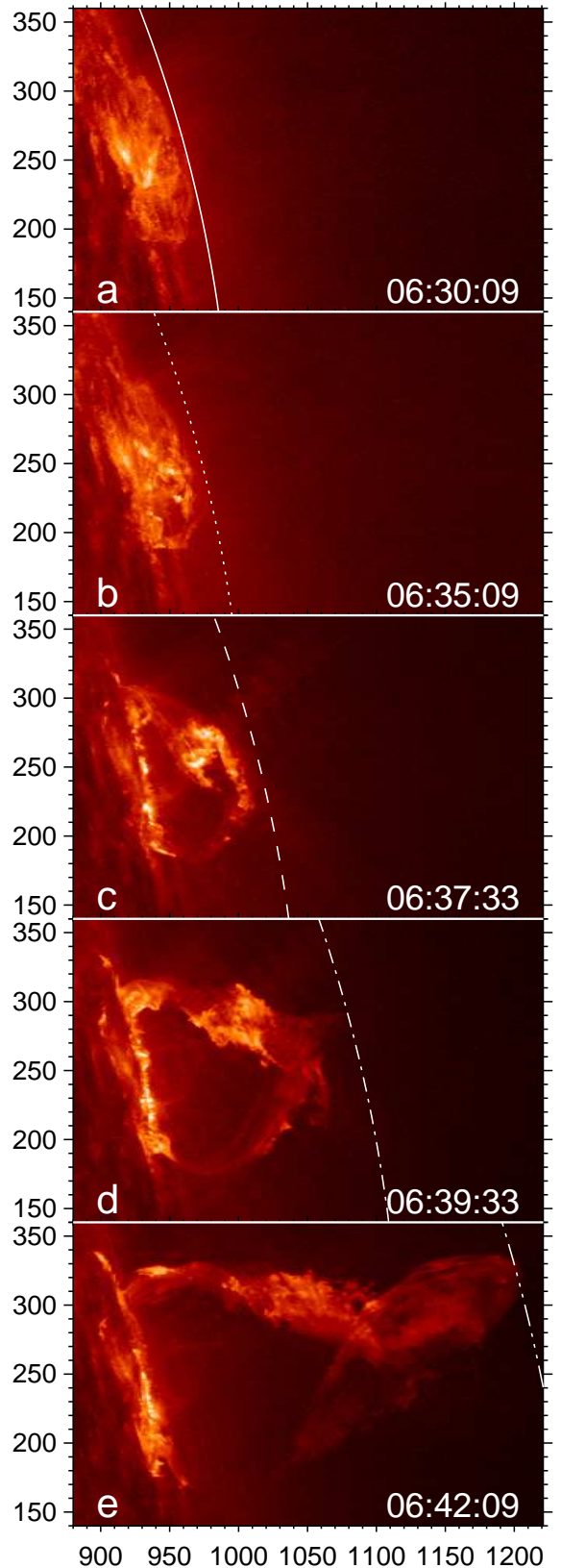


Figure 13: Prominence eruption on 16 March 2016 in the SDO/AIA 304 Å images. The arcs outlining the top of the erupting prominence correspond to the kinematic curves presented in Figure 14. The axes indicate the distance from solar disk center in arcseconds.

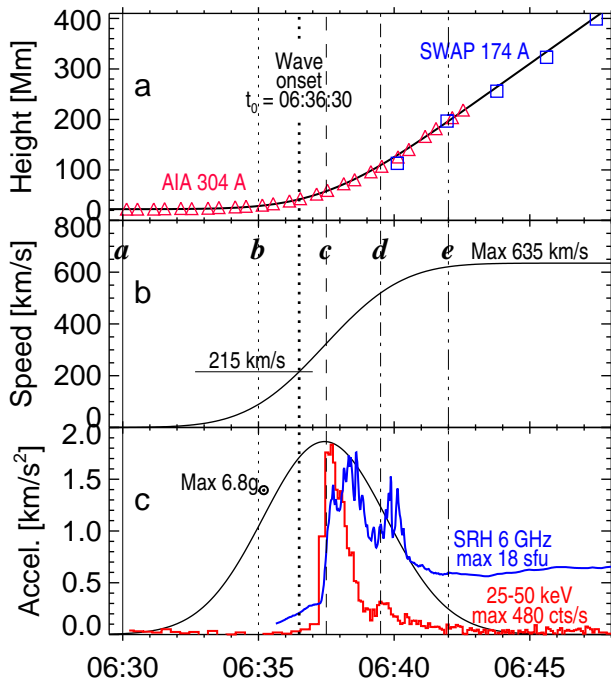


Figure 14: Kinematics of the erupting prominence on 16 March 2016. a) Height–time plot measured from the SDO/AIA 304 Å images (triangles) and Proba 2/SWAP 174 Å images (squares). The analytic curve was fit to the measurements (see the text). b) Velocity–time plot. The vertical lines of different styles denote the times of the images in Figure 13; its panels are indicated by the bold-italic labels. c) Acceleration–time plot. The red curve shows the 25–50 keV flux (Fermi/GBM). The blue curve shows the 6 GHz flux (SRH).

of view with the *Sun Watcher using Active Pixel system detector and image processing* (SWAP: Berghmans et al., 2006) onboard the PROBA 2 micro-satellite. Although the rising prominence is barely detectable in the SWAP images, they allowed us to expand the measured height interval almost twice. The results are shown in Figure 14a, where the red triangles represent the measurements from AIA images, and the blue squares correspond to the measurements from SWAP images. The refinement of the measurements did not affect the results considerably.

The height–time dependence in Figure 14a is simple: The initial speed is close to zero; then the slope (i.e. speed) monotonically increases and finally becomes nearly constant. The acceleration determines the curvature of the bend in the height–time plot; it works within a limited interval and does not change the sign. The double integration in the transition from the acceleration to the height–time plot makes the role of a particular shape of the acceleration pulse negligible. Here we use a Gaussian acceleration pulse, adjusting its parameters to match the height–time points measured. The variations in the height, velocity, and acceleration of the prominence top are calculated in this way by integration of a smooth analytic function instead of a problematic differentiation of scattered measured points. The method of the analytic fit to the measured data proved its reliability and accuracy in several studies (Gallagher et al., 2003; Sheeley et al., 2007; Wang et al., 2009; Alissandrakis et al., 2013) and was also successfully used in the cases, when the

kinematics was more complex (e.g. Grechnev et al., 2011b, 2013a, 2016; Kuzmenko and Grechnev, 2017).

The velocity and acceleration of the prominence top found using this method are presented in Figures 14b and 14c. For comparison, Figure 14c also shows the temporal profiles of the burst recorded by the SRH at 6 GHz and by the *Fermi Gamma-ray Burst Monitor* (GBM: Meegan et al., 2009) in HXR. The maximum velocity acquired by the prominence top was  $635 \text{ km s}^{-1}$ , much higher than the sound speed. Hence, plasma ahead of the erupting prominence could not efficiently flow away which results in the development of a compression region. The acceleration reached  $1.86 \text{ km s}^{-2}$ , or 6.8-fold solar gravity acceleration ( $g_{\odot} = 274 \text{ m s}^{-2}$  at the solar surface).

Although the peaks of the HXR burst and acceleration pulse occurred nearly simultaneously, the prominence started accelerating at least two minutes earlier than the main sharp rise of the microwave and HXR bursts. Thus, microwave SRH observations and HXR data indicate that efficient electron acceleration was initiated by the prominence eruption. We observed the earlier development of the eruption process with respect to non-thermal flare emissions in different events, where a clear lag of order 100 s was present between the acceleration pulse and flare bursts (Grechnev et al., 2011b, 2013a, 2016). This relation does not support an attractive idea of a feedback relationship between the CME motion and the flare energy release (Vršnak, 2008).

### 5.3. EUV Wave

With a strong acceleration up to  $6.8g_{\odot}$ , the erupting prominence must have produced a magnetohydrodynamic (MHD) wavelike disturbance. Its initial propagation velocity is determined by the local fast-mode speed ( $v_{\text{fast}}$ ), which is high above an active region (typically  $v_{\text{fast}} > 1000 \text{ km s}^{-1}$ ). Away from the wave origin, the  $v_{\text{fast}}$  in the environment decreases both upwards and laterally, reaching about  $200 \text{ km s}^{-1}$  above the quiet Sun. When a high-speed disturbance enters the environment of a considerably lower  $v_{\text{fast}}$ , its profile steepens, and the disturbance rapidly becomes a shock wave. In this impulsive-piston scenario, the shock formation is determined mainly by the maximum acceleration of the eruption and the  $v_{\text{fast}}$  falloff away from the eruption region and does not depend on the relation between the eruption speed and the local  $v_{\text{fast}}$  in the environment (Afanasyev et al., 2013).

The disturbance excited by the erupting prominence is visible in the 2016-03-16\_AIA171\_211.mpg movie, which presents nearly simultaneous AIA 171 Å and 211 Å images. The diffuse coronal background was removed from the 171 Å images on the left. The 211 Å running-difference images on the right show the propagating disturbance. Unlike some other events, no manifestations of a rim are detectable around the erupting prominence in either the 211 Å running differences or the filtered 171 Å images, while the latter could reveal the rim most clearly (see, e.g., Grechnev et al., 2016), if it had been present.

The 211 Å running-difference images in the movie reveal the following. At about 06:35, faint structures above the erupting prominence appeared, which reveals their displacement caused by the early rise of the prominence (conspicuous due to its black

appearance in the enhanced-contrast images). A bright compression region above the prominence top appeared at 06:37, when its velocity reached  $300 \text{ km s}^{-1}$ , and expanded at 06:38, when the velocity became  $400 \text{ km s}^{-1}$ . A fast disturbance propagated during 06:39–06:42 along transequatorial loops connecting the parent active region with remote southern regions, indicating a high Alfvén speed in the loops. Then, a large-scale brightening (EUV wave) is visible that propagates along the surface and above the limb on the southwest.

To analyze the EUV wave propagation quantitatively, we invoke its approximate analytic description, which was used in our previous studies of several events (Grechnev et al., 2008, 2011b,a, 2013a, 2014a, 2015, 2016, 2017b) to follow various shock-wave signatures such as EUV waves, Type II bursts, and wave traces ahead of CMEs. This approach uses a power-law density model

$$n(x) = n_0(x/h_0)^{-\delta} \quad (1)$$

where  $x$  is the distance from the eruption center,  $n_0$  is the density at a distance  $h_0 = 100 \text{ Mm}$ , which is close to the scale height, and the density falloff exponent  $\delta$  generally depends on the wave propagation direction. The development of a compression region during the eruption before the appearance of the shock wave strongly disturbs the corona, making standard coronal density models in the near zone inadequate, while the corona remains quiet in the far zone. The power-law density model (1) describes this situation acceptably: with  $x \approx r - R_\odot$  being the height from the photosphere,  $n_0 = 4.1 \times 10^8 \text{ cm}^{-3}$ , and  $\delta = 2.6$ , it is close to the equatorial Saito model (Saito, 1970) within  $\pm 30\%$  at the distances exceeding  $260 \text{ Mm}$ , providing higher densities at lesser heights.

A blast-wave-like shock, which spends its energy to sweep up and extrude the plasma from the volume it occupied previously, has a power-law kinematics,  $x(t) \propto t^{2/(5-\delta)}$  versus time  $t$  (Grechnev et al., 2008). We use this equation in the form

$$x(t) = x_1[(t - t_0)/(t - t_1)]^{2/(5-\delta)}, \quad (2)$$

where the starting estimate of the wave onset time,  $t_0$ , can be taken equal to the maximum acceleration time, and  $x_1$  is the distance from the eruption center to one of the wave fronts observed at time  $t_1$ . Then, we adjust in sequential attempts the  $\delta$  and  $t_0$  parameters to reach a best fit of the wave propagation. The density falloff exponent  $\delta$  determines the curvature of the distance–time plot: with a maximum value  $\delta = 3$  it has a linear shape, and a decrease of  $\delta$  increases the curvature of the plot.

The shape of the global shock-wave front is close to an ellipsoid (Grechnev et al., 2011a, 2014a, 2017b; Kwon et al., 2014, 2015; Rouillard et al., 2016) with a ratio of the axes not much different from unity; for simplicity we consider a spheroid, i.e. ellipsoid of revolution. Its axis corresponds to the acceleration vector of the eruption. If the large-scale  $v_{\text{fast}}$  distribution is strongly inhomogeneous (e.g. because of the presence of a large coronal hole), then the orientation of the axis gradually displaces toward the region of a higher  $v_{\text{fast}}$  (Grechnev et al., 2011a, 2013a). The shock front is “hard” like an ocean tube wave, being governed by the global wave expansion and does

not depend on local inhomogeneities in the  $v_{\text{fast}}$  distribution. For this reason, the description of the near-surface wave propagation with Equation (2) corresponds to an intermediate value of  $\delta_S$  between zero expected for a constant density and  $\approx 2.6$  typical of the radial direction (we usually observed  $\delta_S \approx 2.0$  for EUV waves). The stronger near-surface retardation causes a tilt of the shock front sometimes observed (Hudson et al., 2003; Warmuth et al., 2004b). Local inhomogeneities in the  $v_{\text{fast}}$  distribution over the solar surface determine the brightness of the EUV wave (Grechnev et al., 2011a), while larger inhomogeneities affect its propagation velocity and cause its reflection and refraction (e.g. Veronig et al., 2008; Gopalswamy et al., 2009; Grechnev et al., 2011b).

Keeping in mind these circumstances, we calculated the global shock-wave fronts and their surface skirt (EUV wave). They are shown in Figure 15b–i and the 2016-03-16\_AIA211\_wave.mpg movie on top of the AIA 211 Å running differences. Figure 15a presents an averaged pre-event AIA 211 Å image, which shows active regions (green in the movie) and coronal holes (blue in the movie). The elliptic arcs on the surface are small circles parallel to the equator of the sphere, whose pole coincides with the eruption site. The distances are measured from the pole to the small circles along the great circle.

Figure 15 and the movie reveal a complex character of the EUV wave. From 06:37 to 06:53, the calculated ellipses bound its outermost signatures in both hemispheres, except for the mentioned southwards fastest disturbance on the west above the limb. After 06:53, the EUV wave is conspicuous southwest from the extended southern coronal hole, while large-scale inhomogeneities complicate and hamper its propagation farther in the northern hemisphere. Overall, while the calculated ellipses represent, on average, the global expansion of the wave dome above the limb and its surface trail, the presence of active regions and coronal holes governs the propagation and appearance of the EUV wave according to the associated inhomogeneities in the  $v_{\text{fast}}$  distribution over the solar surface. Their influence corresponds to the expectations for a mast-mode wave.

Figure 16 presents the kinematics used to outline the wave signatures in Figure 15 and the movie. The wave onset time was refined to fit the EUV wave propagation,  $t_0 = 06:36:30$  (the vertical thick-dotted line in Figure 14). The density falloff exponents for the radial direction  $\delta_C = 2.5$  and for the near-surface propagation  $\delta_S = 2.4$  almost coincide in this case.

The EUV wave velocity in Figure 16b monotonically decreased by 80% within an interval shown in Figure 15. This behavior with a strong deceleration is consistent with a pioneering result of Warmuth et al. (2001) and several later studies, but is not exhibited by all EUV transients (e.g. Warmuth et al., 2004a,b, 2005; Muhr et al., 2011, 2014; Nitta et al., 2013b; Long et al., 2017; see Warmuth, 2015 for a review). In our previous case studies, we observed exactly this behavior for shock-associated EUV waves. On the other hand, if the EUV wave properties had been studied solely from signatures in the images, especially by means of an automated detection algorithm, then understanding its kinematics would be difficult.

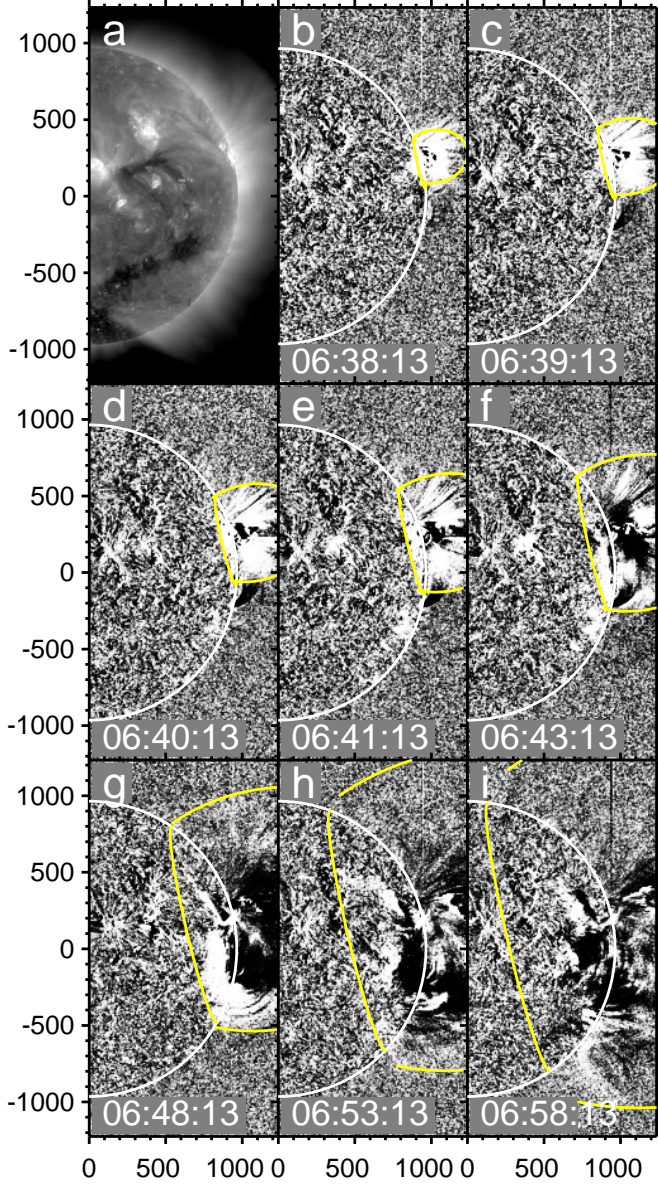


Figure 15: a) Average of four AIA 211 Å images on 16 March 2016 from 06:30 to 06:33. b–i) EUV wave in running-difference AIA 211 Å images. The white circle denotes the solar limb. The arcs outline the wave front. The axes indicate the distance from solar disk center in arcseconds.

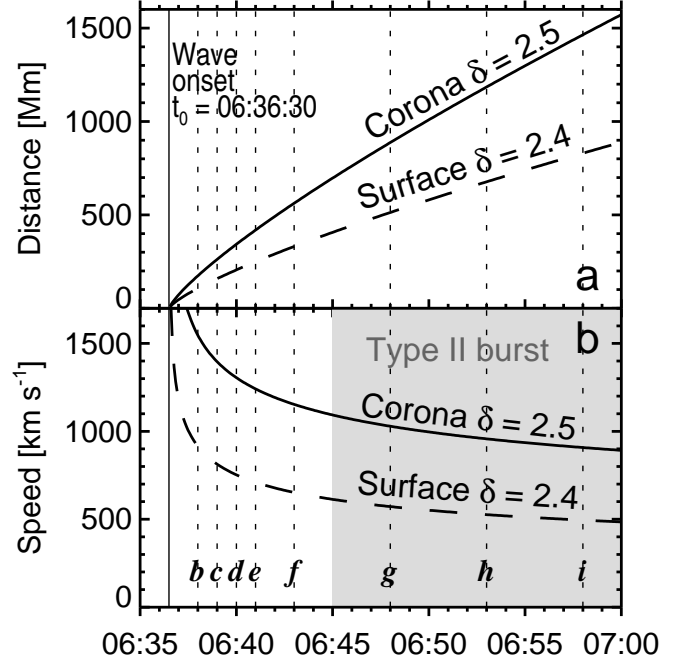


Figure 16: Distance–time (a) and velocity–time (b) plots of the EUV wave. The wave propagation in the radial direction (up) is represented by the solid curve, and the dashed curve represents its surface trail. The vertical solid line denotes the wave onset time. The vertical dotted lines denote the times of the images in Figure 15 whose panels are indicated by the bold-italic letters. The shading in panel b denotes the observation interval of the Type II burst (continued afterward).

#### 5.4. Type II Burst

While the EUV wave reveals a fast-mode disturbance, which was most likely super-Alfvénic, its shock-wave regime is not obvious. A commonly accepted evidence of a shock wave is a Type II radio burst. An important property of Type II bursts is their narrow-band emission. To ensure it, the source should be compact; otherwise, a large shock front crossing a wide range of plasma densities could only produce a drifting continuum (Knock and Cairns, 2005). An appropriate source of a Type II emission is a distinct narrow structure, i.e. coronal streamer (Uralova and Uralov, 1994; Reiner et al., 2003) that was confirmed in imaging meter-wave observations of Type II sources (Feng et al., 2013; Chen et al., 2014; Du et al., 2014; Lv et al., 2017). A Type II burst can be emitted from a remote streamer crossed by a flank of a quasi-perpendicular or oblique shock or from a streamer located above the eruption region crossed by the front of a quasi-parallel shock. The former case probably corresponds to a typical situation, and the infrequent latter case is characterized by a considerably faster drift (Grechnev et al., 2014a, 2016). In either case, the shock crossing the streamer deforms its current sheet that produces a flare-like process running along the streamer together with the intersection point. This scenario has shed light on various structural properties of Type II bursts (Grechnev et al., 2011b, 2014a, 2015, 2016).

Figure 17 shows a dynamic spectrum combined from the Learmonth and Culgoora spectrographs. The spectrum presents a strong Type V burst co-temporal with the main burst in HXR

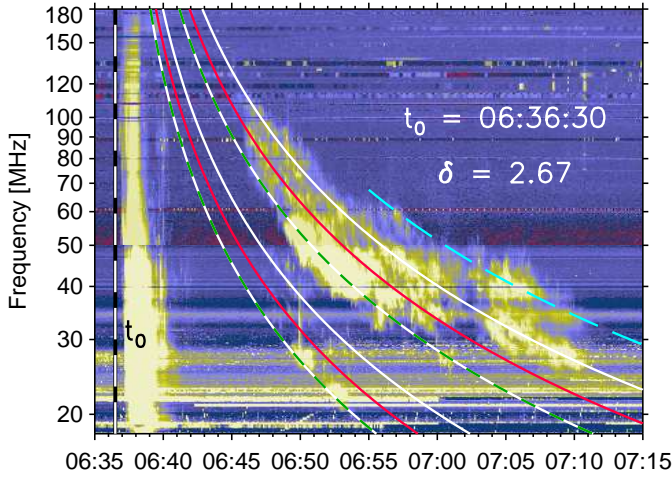


Figure 17: Dynamic spectrum of the metric radio burst composed from the Learmonth and Culgoora data. The vertical dashed line denotes the wave onset time  $t_0 = 06:36:30$ . The curves of different line styles and colors outline different bands in the Type II structure; the paired curves outline the fundamental and harmonic emissions. All of the curves correspond to the same  $t_0$  and density falloff exponent  $\delta = 2.67$ , suggesting a single shock front crossing a few emitting structures.

and microwaves in Figure 14c followed by a faint Type III burst at 06:40 corresponding to a minor burst. At 06:46, a Type II burst with a complex structure started. Its fundamental-emission band was strongly suppressed, while the harmonic emission consisted of at least three indistinct lanes. A fine Type III-like structure of the lanes is detectable suggesting acceleration of electrons in the running flare-like process.

To analyze the frequency–time drift of the Type II burst, we use the approach described in the preceding section. We choose a reference point of a Type II band on the dynamic spectrum at time  $t_1$  with a frequency  $f_1$ , convert the frequency into the density  $n_1$  assuming the fundamental emission at the plasma frequency  $f_p = 9 \times 10^4 n^{1/2}$  or its second harmonic  $2f_p$ , and then convert  $n_1$  into the distance  $x_1$  using the power-law density model (1). Taking starting estimates for  $t_0$  and  $\delta$ , we calculate the trajectory using Equation (2), convert it to the frequency and plot on top of the dynamic spectrum. The values of  $t_0$  and  $\delta$  are optimized in sequential attempts to reach the best fit of the trajectory to bright Type II signatures (see Grechnev et al., 2014a, 2017b for details). If a Type II band is clearly defined, then two reference points can be chosen. The `type_II_fit.mpg` movie presents the adjustment of the Type II trajectory using this example. Here the only variable is  $\delta$ , which governs the curvature of the trajectory, and its optimal value  $\delta = 2.67$  determines  $t_0 = 06:36:30$ , the same as for the EUV wave. The difference between the  $\delta = 2.67$  and  $\delta_C = 2.50$  for the coronal wave (Figure 16) can be due to different directions.

With  $t_0$  and  $\delta$  estimated for a single harmonic band, the trajectories for different bands at both harmonics were calculated by referring to different  $f_1$  at the same  $t_1$  and plotted in Figure 17 with different line styles and colors (same for each harmonically related pair). An extra band with the same  $t_0$  and  $\delta$  appeared at 06:55:00. The coincidence of the wave onset times and even the density falloffs for all of the bands indicates their

common origin related to the same shock front.

The structure of the Type II burst does not resemble the band-splitting, and this effect conventionally interpreted by the emission upstream and downstream of the shock front cannot account for more than two bands. It is also difficult to relate this structure to a single bow-shock-associated source ahead of the CME nose, which can only produce a single or split harmonic pair of bands. Instead, the presence of several pairs of bands points at a corresponding number of compact sources not much different from each other. Most likely, they were located at the flanks of the coronal wave and none ahead of the CME nose because of their similar drift rates with the same  $\delta$ . This assumption is supported by the strong absorption of the fundamental emission along the line of sight either in a long column of the corona in front of the Type II sources above the west limb, or a dense structure such as the base of the streamer belt, or both.

The appearance of the EUV wave in Figure 15 and the 2016-03-16\_AIA211\_wave.mpg movie is not different before the start of the Type II burst (06:45:00) and after it. The wave velocity in Figure 16b monotonically decreased, being in the first panels of Figure 15 most likely higher than the ambient fast-mode speed both along the surface and in the radial direction. The Type II burst started when the wave considerably decelerated (shading in Figure 16b). All of these facts indicate that the lag of the Type II burst behind the wave onset time is determined by the distance required for the shock front, which already exists, to propagate until the encounter with a streamer, which can produce the Type II emission, and does not depend on the relation between the velocity of the wave or ejecta and the ambient fast-mode speed. Long et al. (2017) found the delay of a Type II burst relative to the EUV wave onset to be typical.

In summary, both the EUV wave and Type II burst point to the same wave onset time at 06:36:30. The velocity of the prominence top, which excited the wave, was  $215 \text{ km s}^{-1}$  at that time (the thick dotted line in Figure 14b). It should be noted that Equation (2) used in our measurements was obtained for a spherical blast wave expanding from a point-like source (Grechnev et al., 2008). A real wave exciter can be spatially extended, which might shift the actual wave onset time. In the radial direction corresponding to the eruption, the wave represented by the solid curve in Figure 16 travels, e.g., 20 Mm in 6 s and 50 Mm in 20 s. Even with the largest time shift the velocity of the prominence top in Figure 14b did not exceed  $300 \text{ km s}^{-1}$ , being certainly sub-Alfvénic. On the other hand, the wave started close to the maximum acceleration time in Figure 14c that occurs in the impulsive-piston shock excitation scenario.

### 5.5. White-Light Transient

The eruption produced a decelerating CME. According to the online CME catalog ([https://cdaw.gsfc.nasa.gov/CME\\_list/](https://cdaw.gsfc.nasa.gov/CME_list/); Yashiro et al., 2004), it had a central position angle of  $265^\circ$ , an average speed of  $592 \text{ km s}^{-1}$ , and acceleration of  $-22.4 \text{ m s}^{-2}$ . Figure 18 presents the wave traces in contrasted LASCO-C2 running-difference images. The radii of the

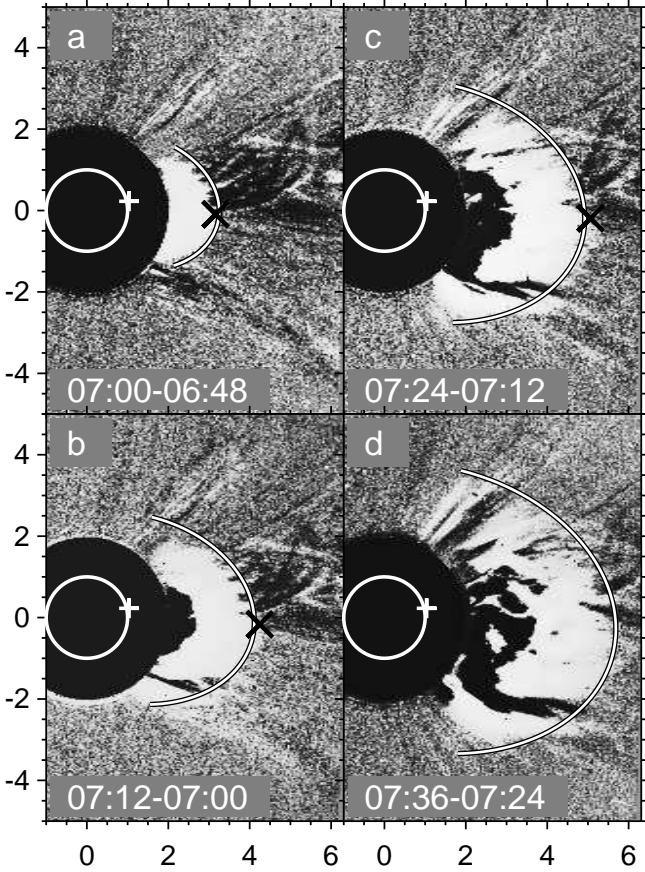


Figure 18: Wave traces on 16 March 2016 in LASCO-C2 images (running differences). The thick white circle denotes the solar limb. The small white crosses denote the eruption center. The larger slanted black crosses in panels a–c denote the measurements in the CME catalog. The arcs outline the wave front. The axes indicate the distance from solar disk center in solar radii.

white-on-black arcs were calculated from the decelerating wave kinematics in Figure 16a with the same  $t_0 = 06:36:30$  and  $\delta = 2.5$ . The arcs match most of the wave traces, which are manifested in the partial halo enveloping the CME body and deflections of the coronal rays. The arcs are close to the measurements in the CME catalog denoted by the black slanted crosses.

Figure 19 shows the CME structure in non-subtracted C2 images. The white arcs correspond to wave traces. Neither the frontal structure nor cavity are pronounced. The black-dashed arcs outline the main part of the CME body (core) with a helical structure inherited from the erupted prominence. It seems to be more complex than one expects for a perfect flux-rope structure.

Figure 20 presents the kinematical plots for the wave (solid) and CME body (dashed) along with the measurements from the CME catalog (symbols). The way to obtain the wave kinematics has been discussed in detail. It is more complex to infer the kinematics of the CME body, which is determined by different processes at different stages of its development.

The kinematics of the erupting prominence governed by an MHD instability was measured in Section 5.2 using the fit with a Gaussian acceleration pulse (Figure 14). When the instability expires, the CME expands for some time freely and self-

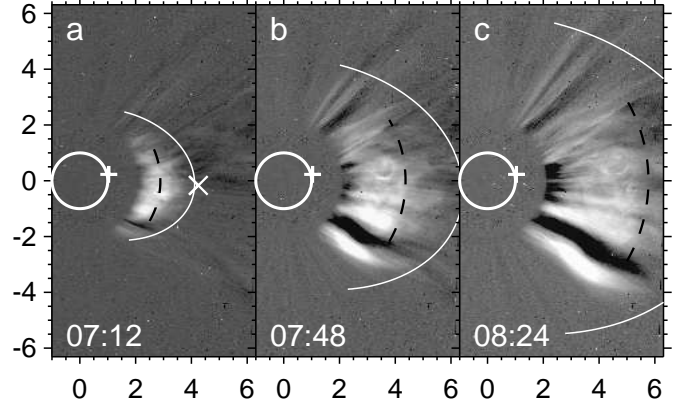


Figure 19: The CME on 16 March 2016 in LASCO-C2 images (fixed-base ratios). The thick white circle denotes the solar limb. The small crosses denote the eruption center. The slanted cross in panel a denotes the measurement in the CME catalog. The white solid arcs outline the wave front, and the black-dashed arcs outline the flux-rope-like structure. The axes indicate the distance from solar disk center in solar radii.

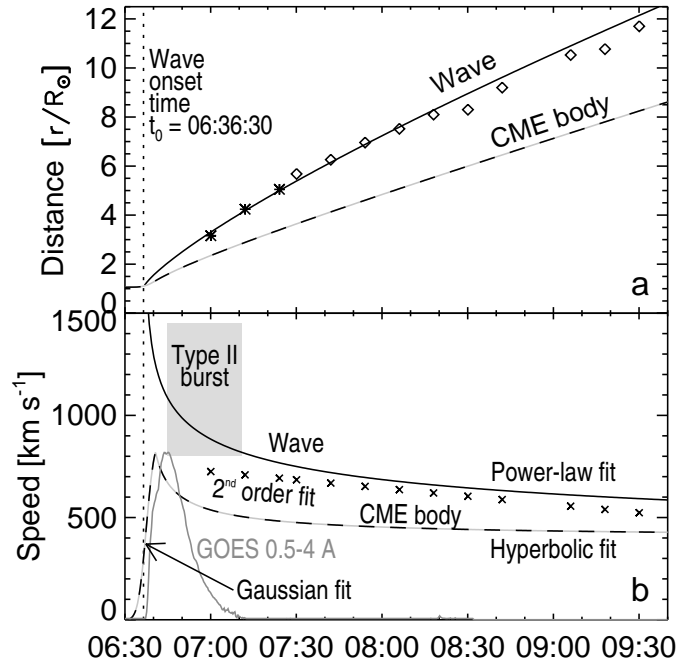


Figure 20: Overall kinematical plots of the wave signatures (solid) and CME body (dashed): a) heliocentric distances versus time, b) velocity–time plots. The symbols represent the measurements in the CME catalog. The gray curve in panel b is the GOES 0.5–4 Å flux scaled to match the plot of the CME body. The shading in panel b shows the interval when the Type II burst was observed.

similarly (Cremades and Bothmer, 2004). Eventually, the CME kinematics should be determined by the aerodynamic drag from solar wind (Chen, 1989, 1996; Vršnak and Gopalswamy, 2002), whose dominance is expected beyond  $15 R_{\odot}$  (Vršnak, 2006; Temmer et al., 2011). As Kuzmenko and Grechnev (2017) showed, exceptions do occur, and nevertheless the CME expands nearly self-similarly at moderate distances from the Sun.

The self-similar character of the CME expansion is determined by the fact that the magnetic propelling and retarding forces, plasma pressure and gravity decrease after the termination of the initial instability by the same factor inversely proportional to the distance from the eruption center squared (except for the drag). The theory of self-similar expansion of solar CMEs was initially developed by Low (1982). A description of a self-similar expansion convenient in the analysis of observations was proposed by Uralov et al. (2005). From their formulas, the instantaneous velocity  $v$  can be related to the distance  $R$  from the expansion center (Grechnev et al., 2008):

$$v^2 = v_0^2 + (v_{\infty}^2 - v_0^2)(1 - R_0/R), \quad (3)$$

where  $R_0$  is the initial position of the CME and  $v = dR/dt$  and  $v_0$  and  $v_{\infty}$  are its initial velocity and the asymptotic final velocity in the self-similar expansion stage. With a simple form, Equation (3) cannot be integrated explicitly; the formulas for the time versus distance dependence are cumbersome. They can be found in Grechnev et al. (2014a). The properties of the self-similar plots correspond to those of hyperbolic functions. Acceleration in the self-similar regime cannot increase by the absolute value and therefore this approach does not apply to the CME's initial lift-off during the impulsive acceleration stage.

We concatenated the kinematics of the erupting prominence fitted with a Gaussian acceleration (Figure 14) with the self-similar kinematics of the CME. The rising prominence forces to expand closed coronal structures above it, which are expected to be ahead but were not observed. To take account of their presence in LASCO images, the prominence velocity was increased by 40%. The resulting velocity–time plot for the CME body is presented in Figure 20b by the dashed curve. Its integration provided the distance–time plot in Figure 20a used to calculate the radii of the black-dashed arcs outlining the CME body in Figure 19. The 2016-03-16\_C2\_ropewave.mpg movie shows the CME body and wave in the images, whose field of view is scaled according to the measured kinematics to fix the visible size of the transient.

Zhang et al. (2001) established similarity between the CME velocity variations and the rise phase of the GOES SXR flux and found indications of similarity between the CME acceleration and the HXR burst confirmed by Temmer et al. (2008). The similarity between the HXR and the derivative of the SXR flux is really expected due to the Neupert effect (Neupert, 1968). A case study by Grechnev et al. (2016) demonstrated a close correspondence between the kinematics of an erupting structure and X-ray emissions, which were delayed by about 2 minutes that resembles the situation in this event. There is the similarity indeed between the rising parts of the CME velocity plot and

the GOES 0.5–4 Å flux (gray in Figure 20b), which lags behind the velocity by 140 s.

The self-similar plots resemble the CME kinematics expected for a drag-dominated situation, whereas the responsible forces are quite different (the similarity is also possible for gradually-accelerating slow CMEs). For this reason, if a drag-based model acceptably describes the CME kinematics, then this result does not guarantee the importance of the drag.

The measurements in the CME catalog are carried out for the fastest feature of a transient, being therefore most likely related to a wave ahead of the CME body, if it is present. Figure 20a confirms the agreement between these measurements and our curve. To find the velocity of a transient, the linear and second-order fit are used in the CME catalog. The latter is presented in Figure 20b by the slanted crosses, whose difference from our power-law fit is mostly not large. The difference increases at shorter distances that results in a strong underestimation by the second-order fit of the wave velocity during its initial evolution hidden by the occulting disk of LASCO-C2.

The interval when the Type II burst was observed is denoted in Figure 20b by the gray shading. The Type II burst ceased by 07:11, when the wave velocity decreased to about  $800 \text{ km s}^{-1}$ , and did not extend into the frequency range below 14 MHz. These circumstances indicate that the decelerating shock decayed at about this time into a weak disturbance. The maximum heliocentric distance at that time was  $4.2 R_{\odot}$  for the wave front and  $2.8 R_{\odot}$  for the CME body, whose velocity was  $500 \text{ km s}^{-1}$ . The shock wave had not changed to the bow-shock regime, because the trailing CME body was sub-Alfvénic.

### 5.6. Implication to the Near-Earth Proton Enhancement

The SXR emission of this eruptive flare up to C2.2 level had an impulsive time profile with a duration of 23 minutes (Figure 21a). At about the time of the event, a weak near-Earth proton enhancement started (Figure 21b). The proton flux reached about 1 pfu in the  $> 10 \text{ MeV}$  integral channel, was detectable in the averaged  $> 50 \text{ MeV}$  channel, and possible in the  $> 100 \text{ MeV}$  channel, exceeding the  $3\sigma$  level above the background around 11:00. Figure 21a also reveals a minor secondary SXR enhancement during 07:45–08:05 marked on the 1–8 Å plot by a thin vertical bar. A group of metric Type IIIs around 08:00 extending to lower frequencies in the Wind/WAVES spectrum corresponds to this minor event, while neither SOHO/LASCO nor STEREO-A/COR1 show any additional CME. The proton event already started at that time and was therefore caused by the eruptive C2.2 event in AR 12522 observed by the SRH, while the minor event around 08:00 was unlikely important.

This impulsive flare accompanied by a modest microwave burst of 18 sfu seems to be too weak to produce the proton event; the most probable candidate for its source is the shock wave. It appeared during the flare rise, being able to accelerate protons considerably earlier than usually assumed, and decayed soon, having not changed to the regime of the CME-driven bow shock. These circumstances show that a widely accepted view relating solar energetic particles with CME-driven shocks, which develop at considerable heights, needs refinement.

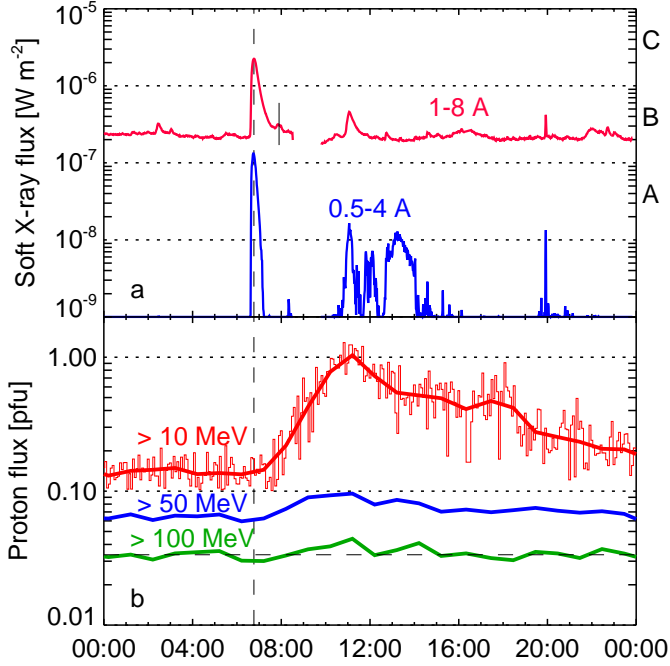


Figure 21: GOES plots of SXR fluxes (a) and integral proton channels (b) recorded on 16 March 2016. The histogram-like thin line in panel b presents the original 5-minute data on  $> 10$  MeV protons. The thick lines present the proton fluxes summed over 1 hour. The vertical dashed line marks the peak time of the SXR flux. The horizontal dashed line shows the background level in the  $> 100$  MeV proton channel averaged over the preceding and next days.

## 6. Discussion

### 6.1. Summary on the Eruptions Observed with the SRH

Being not able to resolve the spatial structure of eruption regions, the SRH detects the occurrence of many eruptions, whose energy and spatial size can be very small, and locates their positions on the Sun. The eruptions presented here were revealed in one of three ways: i) from microwave depressions shown in Section 3, ii) by direct SRH observations of the eruptions, as was the case on 1 May 2017 in Section 4, and iii) by the examination of the eruptive flare observed by the SRH on 16 March 2016 (Section 5). In all of these cases, the SRH provides the pointing to the events, which are analyzed using data acquired by a number of different instruments. This is a usual way to study complex solar events.

The microwave depressions shown in Section 3 as well as the negative bursts on 9 August 2016 in AR 12574 (N04 E59) presented by Lesovoi et al. (2017) occurred not far from the limb. The intensity depressions were accompanied by changes in the polarization that indicates the screening of microwave sources, which had a considerable polarization, i.e. gyromagnetic sources. In all of these cases, the screening was caused by low-temperature jets, which occurred near sunspots indeed. Thus, the jet-like eruptions responsible for the depressions most likely screened polarized sunspot-associated sources. Because the orientations of the jets are not much different from the radial direction, the screening phenomena are favored by the location of the eruptions close to the limb. Deviations in the Stokes V

correlation plots indicate such events, as a cursory analysis of different depressions observed by the SRH confirms.

The events considered in Sections 3 and 4 were associated with jet-like eruptions of different size, where the low-temperature erupted plasma rose and gradually crossed in front of microwave sources, absorbing their emission. The screening caused long-lasting depressions of the microwave emission and changes in its polarization.

As noted in Section 3, multi-frequency observations of microwave depressions provide the basis for plasma diagnostics in erupting structures. Modeling the spectrum of the absorption depths observed at a few frequencies from 1 to 10 GHz allowed estimating parameters of the erupted material responsible for several negative bursts even without images (Grechnev et al., 2008, 2013b; Kuzmenko et al., 2009; Kuzmenko and Grechnev, 2017). These studies used a flat-layered model of a relatively large absorbing cloud of given height, dimensions, temperature, and density, with a possible stable compact microwave source covered. The estimated area screened reached 2–10 % of the solar disk. This approach can also be used to analyze from the SRH data large-scale absorption phenomena, when they would be observed. A narrower SRH frequency range of 4–8 GHz relative to these studies might result in increased uncertainties.

Plasma diagnostics for small eruptions shown in Section 3 is more complex. The fractions of the solar disk covered by the jets in  $304 \text{ \AA}$  were about 0.12 % on 9 September 2017, 0.03 % on 3 August 2017, and 0.05 % on 1 May 2017. The small width of the screen becomes comparable with the size of the microwave source behind it. Here it is necessary to consider additionally the overlap between the narrow jet and a microwave source and to untangle the variations in the opacity of the jet and the changes in the brightness and spectrum of the flaring source. These issues should be addressed in future studies.

Most of the events presented here were associated with jet-like eruptions. A realistic explanation of jets was proposed by Filippov et al. (2009) and Meshalkina et al. (2009) based on three-dimensional magnetic configurations containing coronal null points. Such configurations appear above photospheric magnetic islands surrounded by opposite-polarity regions and resemble an inverted funnel or helmet. If a small flux rope erupts inside the funnel, then its magnetic structure cannot survive when passing at a null point (Uralov et al., 2014), and released plasma flows out as a jet. Eruptions in such configurations are characterized by circular ribbons and impulsive temporal profiles (Masson et al., 2009; Meshalkina et al., 2009). Magnetic islands inside opposite-polarity regions occur very often, and inverted funnels (helmets) are also expected to be quite common configurations. For example, similar configurations are conjectured in Figures 10b and 10d. The roles of such configurations deserve further attention to be paid elsewhere.

### 6.2. Initiation of an Eruption and Development of a Flux Rope

All of the eruptions considered here started developing from below at small heights in the corona. This circumstance is obvious for small eruptions presented in Section 3 and a larger event

on 1 May 2017 shown in Section 4. The situation was also similar in the CME-related 16 March 2016 event. We consider this event in more detail.

The main active structure observed in this event was the eruptive prominence. Its motion started before the HXR and microwave bursts, and the flare ribbons developed later. The chain of events resembles the scenario by Hirayama (1974), in which an MHD instability of an electric current in the prominence drives its lift-off, which stretches associated magnetic fields, forming the current sheet, in which the flare reconnection occurs, and a shock wave is generated ahead of the erupting prominence. None of the SDO/AIA 304 Å, 171 Å, or 211 Å channels, capable of detecting non-flaring structures, reveal within the AIA field of view any larger feature embracing the prominence that could govern its eruption. The behavior of the erupting prominence in Figure 13 and the 2016-03-16\_AIA193\_304\_SRH\_Fermi .mpg movie indicates its own twist instability rather than a reflection of external processes in a larger structure, whose presence is often presumed.

The structure of a pre-eruptive prominence is considerably different from a flux rope, which is rooted to the surface by two ends only. The presence of numerous barbs indicates a multitude of flux-rope-like segments arranged along the magnetic neutral line, each of which is connected to the surface by its ends. A presumable scenario, in which reconnection forms a single flux rope from a multitude of sheared field lines with the appearance of flare loops was theoretically described by Inhester et al. (1992) and Longcope and Beveridge (2007) and got a quantitative support in observational studies (e.g. Qiu et al., 2007; Miklenic et al., 2009).

The MHD instability, which governs the initiation and development of the prominence eruption, is presumably driven by an electric current. In pre-eruptive force-free conditions,  $\nabla \times \mathbf{B} = \alpha \mathbf{B}$ ; the density of the electric current is proportional to the magnetic field strength in a prominence. The field strength in its environment above an active region steeply falls off, as the height increases (e.g. Gary, 2001; Mann et al., 2003). Therefore, the magnetic field and electric current in a prominence are typically stronger near the solar surface than at larger heights. To produce the acceleration with a half-height duration of 5 minutes observed for the erupting prominence in Figure 14, the characteristic Alfvén time in the responsible processes should be much shorter. This would not be possible if the eruption had been governed by a large-scale structure with a weaker magnetic field and longer Alfvén time.

The reconnection process detaches the barbs under the prominence, transforming its structure into the helical structure of the developing flux rope. When its central part is nearly formed, it becomes convex, and the torus instability develops. Figure 13c presents an episode of this stage corresponding to the maximum acceleration measured. Then, the twist instability develops in Figures 13d and 13e, which is often observed, but does not seem to be a necessary phase of the eruption process.

The flux-rope formation is unlikely to occur perfectly and terminate completely in the course of the prominence eruption. Some of the pre-eruptive segments could not recon-

nect. The flux-rope-like structures actually observed (e.g. Cheng et al., 2013; Grechnev et al., 2016) resemble twisted bundles of loops rather than a perfect croissant-shaped structure. Kuzmenko and Grechnev (2017) revealed indications of an ongoing flux-rope formation from twisted core structures during the CME expansion. The structure of the CME body in Figure 19 observed on 16 March 2016 also seems to be more complex than an expected croissant-like flux rope in the CME cavity.

These circumstances indicate that a flux rope forms in the course of a time-extended process. The eruption observed in the extreme ultraviolet is its most impulsive, powerful stage, when a future CME structure develops, while its components have not yet constituted the whole. This fact is essential to determine the actual shock-wave excitation scenario.

### 6.3. Shock Excitation Scenarios

The impulsive-piston shock-wave excitation scenario revealed in Section 5 is not exceptional. The main conditions necessary to realize this scenario are i) more or less impulsive acceleration of an eruptive structure, and ii) pronounced falloff of the fast-mode speed away from the eruption region. These conditions are typical of many events, irrespective of the flare size, and even in cases where non-thermal bursts are not observed in HXR or microwaves. An abrupt eruption is only required, while the presence of a CME is not necessary.

On the other hand, the impulsive-piston scenario is not expected for gradually accelerating CMEs initiated by the eruptions of large quiescent prominences away from active regions. It is also not expected for confined flares independent of their size, that are not associated with expansion of any structures. Such rare flares sometimes occur (e.g. Thalmann et al., 2015; a few major confined flares also occurred in September 2005).

While the shock-wave excitation scenarios have been known for several decades, observations until recently did not allow identifying which one was responsible for the appearance of coronal shock waves (see Vršnak and Cliver, 2008 for a review). The search for their origins has been focused on the “impulsive-piston shock excitation by a flare pressure pulse versus the bow-shock excitation by the outer surface of a super-Alfvénic CME” alternative. A rather obvious scenario outlined in Section 5.3 has been escaping attention, possibly because the flux ropes are assumed pre-existing when the eruptions develop.

Having adopted the “flare versus CME” alternative, one is constrained by its framework and comes to a conclusion about the flare-related shock origin, if its exciter exhibits impulsive properties (e.g. in the case of Moreton waves), or if mismatch between the estimated speeds of the shock and CME is conspicuous, especially if a CME is absent. However, the role of the flare pressure in the shock-wave excitation is unlikely (Grechnev et al., 2011b, 2015) for the following reasons.

1. The plasma density and temperature in flare loops are manifested in their SXR emission. It is gradual in nature and resembles the indefinite integral of the HXR burst (the Neupert effect: Neupert, 1968). On the other hand, the HXR burst roughly corresponds to a sharp acceleration of

an eruption, which produces a strong MHD disturbance, while the plasma pressure in flare loops increases gradually.

2. The plasma pressure in flare loops cannot considerably exceed the magnetic pressure, being compensated by the dynamic pressure of the reconnection outflow. Even if the plasma pressure in a loop becomes comparable with the magnetic pressure ( $\beta \approx 1$ ), the effect is as small as an increase in each of its three dimensions by a factor of  $(\beta + 1)^{1/4}$  (see Grechnev et al., 2006 for details). The increase in the volume of flare loops is basically insufficient to produce an appreciable MHD disturbance outward.

These considerations were verified in case studies of a few events, in which the presence of shock waves was undoubted and their onset times were estimated with certainty (Grechnev et al., 2011b, 2015). The plasma pressure in flare loops estimated from SXR GOES fluxes steadily rose, when the waves were excited near the peak time of the impulsive acceleration of an eruption. The size of the SXR-emitting regions in RHESSI images did not change around the wave onset time. In some events, the wave onset time clearly corresponded to the early rise of an HXR or microwave burst, when the chromospheric evaporation responsible for the plasma pressure in flare loops just started (Grechnev et al., 2013a, 2014a, 2015, 2016). The same situation is seen in Figure 14 in the 16 March 2016 event. The conclusions drawn from the case studies are supported by the statistical independence of the EUV wave occurrence on the flare size (Long et al., 2017).

While the relation between the velocity of an eruption and the ambient fast-mode speed is not important for the initial impulsive-piston excitation of a shock wave, it is crucial for its later evolution. A decelerating shock wave is supplied by the energy from the trailing “piston”, whose role at larger distances really plays the outer surface of the CME body. If it is fast, then the shock wave changes into the bow-shock regime. If the CME is slow, as was the case in the 16 March 2016 event, then the shock decays into a weak disturbance. This occurs most rapidly in confined eruptions without CMEs (but not confined flares). Very rare events of this kind are known indeed, in which EUV waves or Type II bursts, or both were observed (e.g. Shanmugaraju et al., 2006; Magdalenic et al., 2012; Nitta et al., 2014; Grechnev et al., 2014a; Eselevich et al., 2017). Thus, the fact that the vast majority of EUV waves are associated with CMEs (e.g. Biesecker et al., 2002; Long et al., 2017) does not guarantee that every shock wave has an associated CME.

The studies of shock-wave histories are facing heavy observational difficulties. Eruptive structures rapidly acquire high velocities and dramatically lose brightness. Wave signatures possess strong initial deceleration, which is most conspicuous in the first few minutes of their propagation, as Figure 16b exemplifies. At that time, the measurements of the wave propagation and even its detection are hampered by a strong flare emission, while the imaging rate and dynamic range of telescopes are limited. In addition, different objects appear similar to shock-related EUV waves — for example, rising CME structures and quasi-stationary compression regions at their bases

(Zhukov and Auchère, 2004; Chen et al., 2005; Grechnev et al., 2011a; Warmuth, 2015). Finally, a shock wave excited by a sharply erupting structure has a kinematics similar to what is expected for a hypothetical flare blast wave. These circumstances along with the framework of the “flare vs. CME” alternative probably account for the conclusions made in some case studies in favor of flare-ignited shock waves. On the other hand, this alternative and observational difficulties might incline different studies toward the initial bow-shock excitation by the outer surface of a super-Alfvénic CME.

Being constrained by these difficulties, researchers are forced to invoke indirect arguments, which do not always ensure the unambiguous identification of a scenario. These are, for example, the presence of a fast CME that cannot guarantee the bow-shock regime of an associated wave. It is also not certified by the position of the Type II source ahead of a CME, because the Type II emission can originate from the streamer above the eruption region disturbed by the quasi-parallel blast-wave-like shock. Next, a delayed appearance of a Type II burst that does not necessarily mark the onset of the shock formation. On the other hand, the absence of a CME is not evidence of the flare-related shock origin, as mentioned.

#### 6.4. Overview of Actual Shock-Wave Histories

To avoid deceptive indications, it is reasonable to follow the appearance and evolution of shock waves and to measure their propagation from a combined analysis of their various manifestations in different spectral ranges. This way is time-consuming, but provides a highest confidence in adequacy of the outcome. Using this approach, we made a detailed analysis of the shock-wave histories for several events in a manner similar to Section 5, mainly from the extreme-ultraviolet and white-light coronagraph images, dynamic radio spectra, and others (e.g. H $\alpha$  images), if available. The results of these case studies are summarized in Table 1, whose column 15 specifies the article, where they were published.

Table 1 contains 13 events listed chronologically. The kinematics of eruptive filaments or similar structures was measured in 8 events, when it was possible. Two shock waves following each other and merging eventually into a single stronger shock were revealed in four events. Column 1 lists the number of an event with a label “a” or “b” specifying one of the two shocks, if present. Columns 2–5 list the date (in the format of the Solar Object Identifier), peak time, duration, and importance of a flare according to the GOES reports, and column 6 gives its reported position. Columns 7–9 present the estimated wave onset time, the peak time of an HXR or microwave burst, and the onset time of a Type II burst. Columns 10–12 present the CME parameters taken from the online CME catalog ([https://cdaw.gsfc.nasa.gov/CME\\_list/](https://cdaw.gsfc.nasa.gov/CME_list/); Yashiro et al., 2004): the onset time at the limb estimated from a linear fit and second-order fit, and an average speed. Column 13 shows the outcome of the shock-wave history: either a bow shock, or decay. Column 14 lists the peak flux of near-Earth protons > 10 MeV produced by the event (GOES).

The events listed in Table 1 had greatly differing properties. The flares ranged in size from B8.1 to X3.4 and in duration

Table 1: Summary of shock waves studied

No.	Date	GOES			Position	Wave onset time	$T_{\text{peak}}$ HXR or m/w	Type II onset time	CME			Shock outcome	$J_{10}$ [pfu]	Refs
		Peak time	Dur. min	Size					Onset at $1 R_{\odot}$		Speed $\text{km s}^{-1}$			
1	2	3	4	5	6	7	8	9	10	11	12	13	14	15
1	1997-09-24	02:48:00	9	M5.9	S31E19	02:46:50	02:46:50	02:48:40	02:33	00:55 <sup>1</sup>	532	Decay	–	1
2a	2001-12-26	05:40:00	135	M7.1	N08W54	05:04:00	05:04:40	05:08:00	05:06	05:10	1446	Bow	700	2
2b						05:09:00	05:09:00	05:12:00	—— Same ——			—— Same ——		
3	2002-06-01	03:57:00	11	M1.5	S19E29	03:53:40	03:53:40	03:55:30	No coronagraph data			Decay?	–	1
4	2003-11-18	07:52:00	43	M3.2	N00E18	07:41:00	07:42:00	07:47:00	Confined eruption			Decay	–	3
5	2003-11-18	08:31:00	47	M3.9	N00E18	08:14:12	08:16:00	08:15:00	08:13	08:13	1660	Bow	0.7	3
6	2004-07-13	00:17:00	14	M6.7	N13W46	00:14:50	00:15:00	00:16:00	00:02	00:04	607	Decay	1	1,4
7a	2006-12-13	02:40:00	43	X3.4	S06W23	02:23:20	02:25:30	02:26:00	02:25	02:29	1774	Bow	695	5
7b						02:27:20	02:29:00	02:28:00 <sup>2</sup>	—— Same ——			—— Same ——		
8a	2007-05-19	13:02:00	31	B9.5	N07W06	12:50:00	12:51:15	12:52:00	12:56	13:00	958	Decay	–	1
8b						12:56:00	12:57:00	13:01:00	—— Same ——			—— Same ——		
9	2010-01-17	03:56:00	?	X1 <sup>3</sup>	S25E128	03:47:48	No data	03:51:00	03:13	03:45	350	Decay	+	6
10	2010-06-13	05:39:00	14	M1.0	S21W82	05:35:10	05:36:00	05:38:00	05:14	04:56 <sup>1</sup>	320	Decay	–	7
11	2011-02-24	07:35:00	19	M3.5	N19E84	07:29:00	07:30:30	07:34:30 <sup>4</sup>	07:16	07:23	1186	Bow	–	8
12	2011-05-11	02:43:00	60	B8.1	N25W54	02:22:10	02:28:30 <sup>5</sup>	02:27:00	02:26	02:24	745	Decay	0.5	8
13	2016-03-16	06:46:00	23	C2.2	N14W83	06:36:30	06:37:30	06:45:00	06:04	06:21	592	Decay	1	9

<sup>1</sup> Acceleration is uncertain due to either poor height measurement or a small number of height-time measurements (remark from the CME catalog).

<sup>2</sup> Not clear.

<sup>3</sup> Average of the estimates from STEREO-B/EUVI 195 Å images of M6.4 by Nitta et al. (2013a) and X1.6 by Chertok et al. (2015).

<sup>4</sup> Reported 07:37:00 when the Type II structures became clear after overlap with a strong Type III group.

<sup>5</sup> For the derivative of the GOES flux at 1–8 Å.

References: 1. Grechnev et al. (2011b), 2. Grechnev et al. (2017b), 3. Grechnev et al. (2014a), 4. Grechnev et al. (2008), 5. Grechnev et al. (2013a), 6. Grechnev et al. (2011a), 7. Grechnev et al. (2016), 8. Grechnev et al. (2015), 9. Present article.

from 9 to 135 minutes. The average CME speed ranged from  $320 \text{ km s}^{-1}$  to  $1774 \text{ km s}^{-1}$ . Noteworthy was event 4, in which a confined eruption without any CME produced a shock wave, which excited clear large-amplitude oscillations of a remote filament observed in the H $\alpha$  line center and both wings (“winking filament”). The flares in the 13 events had differing morphologies, including two-ribbon flares and flares with circular ribbons. Nevertheless, the shock-wave excitation scenario was the same in all of these events. The wave onset times were close to the peak times of the HXR or microwave bursts or led them by up to 2 minutes (when they were observed), i.e. occurred not later than the flare impulsive phase.

Despite the differences between the events listed in Table 1, shock waves in all of them were initially excited in the same impulsive-piston scenario by sharply erupting filaments or similar structures, as described in Section 5.3. This fact allows combining the results obtained in studies of different events to reveal common properties of these shock waves. The possibility of their flare-related origin was examined in each case study and excluded for the reasons listed in Section 6.3.

Neither was a shock initially excited in any of the events by a super-Alfvénic CME. This result is also expected, because the impulsive-piston shock excitation by a relatively small erupting structure is highly efficient in a medium with a steep falloff of the fast-mode speed away from the eruption region. Hence, the shock appears much earlier than is possible in the bow-shock scenario; the shock waves initially resemble blast waves. While they eventually changed to the bow-shock regime in 4 events in Table 1, this did not affect their early development. The successive appearance in events 2, 7, and 8 of two shock

waves within 6 minutes supports this conclusion, because a single super-Alfvénic CME cannot drive more than one shock.

The initial wave excitation and the CME development turn out to be closely related. Most likely, when an eruption starts, neither a CME nor its flux rope exists in the final form. For example, wave traces in event 10 were revealed inside the developing CME; then the wave passed through its structures and propagated outward like a decelerating blast wave (Grechnev et al., 2016). There is no reason for a concern about the role in the shock-wave excitation of a presumable lateral overexpansion of the CME bubble, which does not yet exist at that time. There was nothing to expand laterally in event 13 (Section 5); nevertheless, the shock wave appeared.

The CME speeds listed in column 12 of Table 1 are related to the plane of the sky, while the CME orientations could be strongly off-plane. The speeds might therefore be underestimated considerably for slow CMEs and moderately for fast CMEs, whose measurements are probably related to nearly spherical wave fronts. With these circumstances, the transition to a CME-driven shock occurs for those CMEs, whose average speed exceeds  $1000 \text{ km s}^{-1}$ . Indeed, to ensure the super-Alfvénic regime, the CME speed should exceed the sum of the Alfvén speed and the solar wind speed. Using the models of the Alfvén speed (Mann et al., 2003) and solar wind speed (Sheeley et al., 1997), Grechnev et al. (2017b) estimated this sum to decrease from  $900 \text{ km s}^{-1}$  at  $5R_{\odot}$  to  $650 \text{ km s}^{-1}$  at  $25R_{\odot}$  (with an established solar wind speed of  $400 \text{ km s}^{-1}$ ). Nevertheless, with a CME speed as high as  $1446 \text{ km s}^{-1}$  in event 2, the bow-shock regime became possible at distances exceeding  $15R_{\odot}$ , while the wave front was still nearly spherical

(Grechnev et al., 2017b).

The transition of a blast-wave-like shock to a CME-driven bow shock corresponds to the change from the regime of the plasma extrusion by the CME body to the regime of the plasma flow around its outer surface, when the aerodynamic drag becomes significant. This change occurring at considerable distances from the Sun determines the shape of a CME-driven shock. It forms from a nearly spherical blast-wave-like shock, while its driver expands in three dimensions (Vršnak and Cliver, 2008; Grechnev et al., 2011b). This makes the bow-shock shape with a Mach cone unlikely and raises a question about its actual shape. An additional consequence of Table 1 is the early shock-wave appearance in events 2 and 7 responsible for major energetic particle events and GLE63 and GLE70. This circumstance should be considered in studies of solar energetic particles.

All of the listed events were associated with decelerating shock waves. The drag should also decelerate fast CMEs, when it becomes important. These circumstances imply that the onset time of a corresponding transient estimated from the second-order fit should generally be somewhat later than that estimated from the linear fit. This pattern mostly holds for the events listed in Table 1, except for those whose observations were of an insufficient quality (events 1, 10 and 12; they were equal for event 5). A positive acceleration estimated in the CME catalog for fast CMEs is probably a result of observational difficulties.

Besides the implications mentioned, there are several other significant consequences of the shock-wave histories discussed. All of them emphasize the importance of systematic studies of coronal shock waves. Statistical studies of EUV waves have recently been made by Nitta et al. (2013b), Muhr et al. (2014), and Long et al. (2017). Some of their conclusions do not agree with each other, probably because of the observational difficulties shown in Sections 5.3 and 6.3. Some others do not seem to be obvious. Our results can shed light on these challenges.

For example, all of these studies stated a poor correspondence between EUV waves and Type II bursts. This seems to be challenging, if the Type II emission originates ahead of a CME, while Muhr et al. (2014) consider them as the EUV waves' driving agent. The situation is different, if Type IIs originate in streamers located away from the eruption region. Such a streamer may exist or may not. If the antiparallel magnetic fields in a streamer are separated by plasma outflow caused, e.g., by a preceding CME, then the streamer cannot generate Type II emission. On the other hand, the visibility of an EUV wave is determined by the ambient fast-mode speed and can be poor, e.g., in coronal holes (Grechnev et al., 2011a; Long et al., 2017). The plasma density depletion caused by a preceding CME also disfavors the detection of an EUV wave. These circumstances might be implicated in the extreme cases of mismatch between EUV waves and Type II bursts shown by Nitta et al. (2014).

The pattern found by Muhr et al. (2014) and Long et al. (2017), with faster EUV waves exhibiting a stronger deceleration, suggests that the highest-speed initial stage of the EUV wave propagation is often not fully measured, as the velocity-time plot in Figure 16b explains. Some causes of a poor EUV

wave visibility are mentioned in the preceding paragraph.

The absence of any relationship between the EUV wave properties and the size of the associated flare stated by Nitta et al. (2013b) and Long et al. (2017) is consistent with our results. Instead, the shock-wave excitation mechanism we are talking about is expected to depend on the acceleration of an eruptive structure that is not easy to measure.

### 6.5. *The Role of the Flare Duration in Soft X-rays*

There is a traditional view relating impulsive flares to narrow or no CMEs and long-decay flares (LDEs) to large CMEs (Kahler et al., 1989). While the authors of this statement talked primarily about major flares ( $\geq$  M1 GOES importance), this pattern obviously holds for minor events presented in Section 3. However, a wide CME on 16 March 2016 discussed in Section 5 developed also in association with an impulsive flare. Some CMEs in Table 1 were also related to impulsive flares. Nitta and Hudson (2001) presented a series of large CMEs, which occurred in association with major impulsive flares in the same active region within 60 hours. Conversely, infrequent major LDEs without any eruptions are known (e.g. Thalmann et al., 2015). Thus, the pattern found by Kahler et al. (1989) seems to represent a tendency, but does not ensure a one-to-one correspondence.

The long decay time in LDEs might be determined by long-lasting reconnection processes occurring typically in the post-eruption phase (Grechnev et al., 2006) or at a late stage of rare confined flares. The conditions favoring such processes still need understanding.

On the other hand, the SXR GOES fluxes might possibly be invoked to find the indications of a probable EUV wave occurrence. According to the Neupert effect, the rise time of the SXR flux should correspond to the acceleration duration of an eruption. Being possibly somehow combined with another parameter of an event, this rise time might characterize its impulsiveness to indicate the magnitude of the acceleration and thus to provide an indication of a probable EUV wave.

## 7. Summary and Conclusion

The T-shaped SRH antenna array with redundant baselines has allowed implementing algorithms to construct correlation plots of the solar radio emission and those to synthesize the images of the Sun without involvement of calibration radio sources. A high sensitivity of the interferometer of about 0.01 sfu in combination with a high dynamic range makes it possible to observe in microwaves without attenuators a wide range of solar activity, from sources of powerful flare bursts down to its faint manifestations associated with microeruptions. The latter occur more frequently, being less studied.

The first observations with SRH have shown its promising opportunities to detect solar eruptions of different energy and spatial size. We have demonstrated three ways to detect the eruptions: i) direct observations of erupted material, ii) observations of microwave bursts as a probable pointing at eruptive

events, and iii) detection of faint eruptive events that manifest as depressions in the total-intensity correlation plots, being accompanied by distinct changes in the circular-polarization plots. Such events can be too weak and small to be detected from any other observations. We have learned from the SRH observations that microwave depressions at 4–8 GHz of this kind are typically polarized. They can be caused by eruptions from the same region repeating in a few hours, and this can occur not once. Such phenomena raise a question what favors energy release in small portions, preventing its accumulation. An answer might shed additional light on preparation conditions and their manifestations for big eruptions which pose a largest space weather hazard. Understanding of the mechanisms responsible for the eruptions of different size, their implication to space weather disturbances as well as development of criteria for their detection is among important future tasks for the multi-frequency SRH.

To carry out detailed studies of solar eruptions, it is reasonable to combine the SRH observations with multi-instrument data from different spectral ranges. This is a typical approach in such studies. Besides the listed opportunities to detect various eruptions, a significant advantage of the SRH observations is promised by their dense frequency sampling: in December 2017, the SRH has started observing first at 15 frequencies, and then at 32 frequencies within the 4–8 GHz range. In February 2018, the time to process each frequency bin has been reduced and reached a planned value of 0.28 s. The time to collect the visibilities at 32 frequencies became about 9 s.

From the multi-instrument analysis of an eruptive event observed by the SRH on 16 March 2016, we have followed the development of a CME and associated shock wave and compared them with expectations from well-known models. This event has demonstrated a direct shock-wave excitation by an erupting prominence without any indications of a cavity or rim bounding it that contradicts their crucial role presumed in some studies. Another highlight of this event is that the shock wave, which was probably responsible for a near-Earth proton enhancement, was not CME-driven and appeared during the flare impulsive phase, when the CME was still in the development stage. Thus, a widely accepted view on the origin of solar energetic particles should be refined. The scenario discussed appears to be typical of various solar eruptions of different importance. We hope our results would be helpful in further studies of solar eruptions, CMEs, and coronal shock waves.

## Acknowledgements

We thank N.V. Nitta and H. Nakajima for fruitful discussions and I.V. Kuzmenko for the RT-2 data. We appreciate our colleagues from the Radio Astrophysical Department and the Radio Astrophysical Observatory in Badary. We are indebted to anonymous reviewers for their valuable remarks. We thank the NASA/SDO and the AIA and HMI science teams; the instrument teams of GOES, RHESSI, the SWAP telescope on the ESA's PROBA2 spacecraft, the NASA's Fermi Gamma-Ray Space Telescope, Culgoora and Learmonth spectrographs of the Australian Space Weather Services, and LASCO on SOHO.

SOHO is a project of international cooperation between ESA and NASA. We thank the team maintaining the CME Catalog at the CDAW Data Center by NASA and the Catholic University of America in cooperation with the Naval Research Laboratory.

The work was performed with budgetary funding of Basic Research program II.16. The results were obtained using the Unique Research Facility Siberian Solar Radio Telescope <http://ckp-rf.ru/usu/73606/>.

## References

- Afanasyev, A. N., Uralov, A. M., Grechnev, V. V., 2013. Propagation of a fast magnetoacoustic shock wave in the magnetosphere of an active region. *Astronomy Reports* 57, 594–602.
- Alissandrakis, C. E., Kochanov, A. A., Patsourakos, S., Altyntsev, A. T., Lesovoi, S. V., Lesovoy, N. N., 2013. Microwave and EUV Observations of an Erupting Filament and Associated Flare and Coronal Mass Ejections. *Publ. Astron. Soc. Japan* 65, S8.
- Berghmans, D., Hochedez, J. F., Defise, J. M., Lecat, J. H., Nicula, B., Slemzin, V., Lawrence, G., Katsyiannis, A. C., van der Linden, R., Zhukov, A., Clette, F., Rochus, P., Mazy, E., Thibert, T., Nicolosi, P., Pelizzo, M.-G., Schühle, U., 2006. SWAP onboard PROBA 2, a new EUV imager for solar monitoring. *Adv. Space Res.* 38, 1807–1811.
- Biesecker, D. A., Myers, D. C., Thompson, B. J., Hammer, D. M., Vourlidas, A., 2002. Solar Phenomena Associated with “EIT Waves”. *Astrophys. J.* 569, 1009–1015.
- Borovik, V. N., 1994. Quiet sun from multifrequency radio observations on RATAN-600. In: Belvedere, G., Rodono, M., Simnett, G. M. (Eds.), *Advances in Solar Physics*. Vol. 432 of Lecture Notes in Physics, Berlin Springer Verlag. pp. 185–190.
- Brueckner, G. E., Howard, R. A., Koomen, M. J., Korendyke, C. M., Michels, D. J., Moses, J. D., Socker, D. G., Dere, K. P., Lamy, P. L., Llebaria, A., Bout, M. V., Schwenn, R., Simnett, G. M., Bedford, D. K., Eyles, C. J., 1995. The Large Angle Spectroscopic Coronagraph (LASCO). *Solar Phys.* 162, 357–402.
- Chen, J., 1989. Effects of toroidal forces in current loops embedded in a background plasma. *Astrophys. J.* 338, 453–470.
- Chen, J., 1996. Theory of prominence eruption and propagation: Interplanetary consequences. *J. Geophys. Res.* 101, 27499–27520.
- Chen, P. F., Fang, C., Shibata, K., 2005. A Full View of EIT Waves. *Astrophys. J.* 622, 1202–1210.
- Chen, Y., Du, G., Feng, L., Feng, S., Kong, X., Guo, F., Wang, B., Li, G., 2014. A Solar Type II Radio Burst from Coronal Mass Ejection-Coronal Ray Interaction: Simultaneous Radio and Extreme Ultraviolet Imaging. *Astrophys. J.* 787, 59.
- Cheng, X., Zhang, J., Ding, M. D., Liu, Y., Poomvises, W., 2013. The Driver of Coronal Mass Ejections in the Low Corona: A Flux Rope. *Astrophys. J.* 763, 43.
- Chertok, I. M., Belov, A. V., Grechnev, V. V., 2015. A Simple Way to Estimate the Soft X-ray Class of Far-Side Solar Flares Observed with STEREO/EUVI. *Solar Phys.* 290, 1947–1961.
- Cliver, E. W., Nitta, N. V., Thompson, B. J., Zhang, J., 2004. Coronal Shocks of November 1997 Revisited: The Cme Type II Timing Problem. *Solar Phys.* 225, 105–139.
- Cornwell, T. J., 2008. Multiscale CLEAN Deconvolution of Radio Synthesis Images. *IEEE Journal of Selected Topics in Signal Processing* 2, 793–801.
- Covington, A. E., 1973. Decrease of 2800 MHz Solar Radio Emission Associated with a Moving Dark Filament before the Flare of May 19, 1969. *Solar Phys.* 33, 439–444.
- Covington, A. E., Dodson, H. W., 1953. Absorption of 10.7-centimetre Solar Radiation during Flare of May 19, 1951. *J. Roy. Astron. Soc. Canada* 47, 207.
- Cremades, H., Bothmer, V., 2004. On the three-dimensional configuration of coronal mass ejections. *Astron. Astrophys.* 422, 307–322.
- Du, G., Chen, Y., Lv, M., Kong, X., Feng, S., Guo, F., Li, G., 2014. Temporal Spectral Shift and Polarization of a Band-splitting Solar Type II Radio Burst. *Astrophys. J. Lett.* 793, L39.

- Eselevich, V. G., Eselevich, M. V., Zimovets, I. V., Sharykin, I. N., 2017. Evidence for shock generation in the solar corona in the absence of coronal mass ejections. *Astronomy Reports* 61, 805–819.
- Feng, S. W., Chen, Y., Kong, X. L., Li, G., Song, H. Q., Feng, X. S., Guo, F., 2013. Diagnostics on the Source Properties of a Type II Radio Burst with Spectral Bumps. *Astrophys. J.* 767, 29.
- Filippov, B., Golub, L., Koutchmy, S., 2009. X-Ray Jet Dynamics in a Polar Coronal Hole Region. *Solar Phys.* 254, 259–269.
- Gallagher, P. T., Lawrence, G. R., Dennis, B. R., 2003. Rapid Acceleration of a Coronal Mass Ejection in the Low Corona and Implications for Propagation. *Astrophys. J. Lett.* 588, L53–L56.
- Gary, G. A., 2001. Plasma Beta above a Solar Active Region: Rethinking the Paradigm. *Solar Phys.* 203, 71–86.
- Gibson, S., 2015. Coronal Cavities: Observations and Implications for the Magnetic Environment of Prominences. In: Vial J.-C., Engvold O. (Ed.), *Solar Prominences. Astrophysics and Space Science Library*, vol 415. Springer, Cham, p. 323.
- Gopalswamy, N., Yashiro, S., Temmer, M., Davila, J., Thompson, W. T., Jones, S., McAteer, R. T. J., Wuelser, J.-P., Freeland, S., Howard, R. A., 2009. EUV Wave Reflection from a Coronal Hole. *Astrophys. J. Lett.* 691, L123–L127.
- Grechnev, V., Uralov, A. M., Kiselev, V. I., Kochanov, A. A., 2017a. The 26 December 2001 Solar Eruptive Event Responsible for GLE63. II. Multi-Loop Structure of Microwave Sources in a Major Long-Duration Flare. *Solar Phys.* 292, 3.
- Grechnev, V. V., Afanasyev, A. N., Uralov, A. M., Chertok, I. M., Eselevich, M. V., Eselevich, V. G., Rudenko, G. V., Kubo, Y., 2011a. Coronal Shock Waves, EUV Waves, and Their Relation to CMEs. III. Shock-Associated CME/EUV Wave in an Event with a Two-Component EUV Transient. *Solar Phys.* 273, 461–477.
- Grechnev, V. V., Kiselev, V. I., Uralov, A. M., Klein, K.-L., Kochanov, A. A., 2017b. The 26 December 2001 Solar Eruptive Event Responsible for GLE63: III. CME, Shock Waves, and Energetic Particles. *Solar Phys.* 292, 102.
- Grechnev, V. V., Kiselev, V. I., Uralov, A. M., Meshalkina, N. S., Kochanov, A. A., 2013a. An Updated View of Solar Eruptive Flares and the Development of Shocks and CMEs: History of the 2006 December 13 GLE-Productive Extreme Event. *Publ. Astron. Soc. Japan* 65, S9.
- Grechnev, V. V., Kochanov, A. A., 2016. The 26 December 2001 Solar Event Responsible for GLE63. I. Observations of a Major Long-Duration Flare with the Siberian Solar Radio Telescope. *Solar Phys.* 291, 3705–3723.
- Grechnev, V. V., Kuzmenko, I. V., Uralov, A. M., Chertok, I. M., Kochanov, A. A., 2013b. Microwave Negative Bursts as Indications of Reconnection Between Eruptive Filaments and a Large-Scale Coronal Magnetic Environment. *Publ. Astron. Soc. Japan* 65, S10.
- Grechnev, V. V., Lesovoi, S. V., Smolkov, G. Y., Krissinel, B. B., Zandanov, V. G., Altyntsev, A. T., Kardapolova, N. N., Sergeev, R. Y., Uralov, A. M., Maksimov, V. P., Lubyshev, B. I., 2003. The Siberian Solar Radio Telescope: the current state of the instrument, observations, and data. *Solar Phys.* 216, 239–272.
- Grechnev, V. V., Uralov, A. M., Chertok, I. M., Kuzmenko, I. V., Afanasyev, A. N., Meshalkina, N. S., Kalashnikov, S. S., Kubo, Y., 2011b. Coronal Shock Waves, EUV Waves, and Their Relation to CMEs. I. Reconciliation of “EIT Waves”, Type II Radio Bursts, and Leading Edges of CMEs. *Solar Phys.* 273, 433–460.
- Grechnev, V. V., Uralov, A. M., Chertok, I. M., Slemzin, V. A., Filippov, B. P., Egorov, Y. I., Fainshtein, V. G., Afanasyev, A. N., Prestage, N. P., Temmer, M., 2014a. A Challenging Solar Eruptive Event of 18 November 2003 and the Causes of the 20 November Geomagnetic Superstorm. II. CMEs, Shock Waves, and Drifting Radio Bursts. *Solar Phys.* 289, 1279–1312.
- Grechnev, V. V., Uralov, A. M., Kochanov, A. A., Kuzmenko, I. V., Prosovetsky, D. V., Egorov, Y. I., Fainshtein, V. G., Kashapova, L. K., 2016. A Tiny Eruptive Filament as a Flux-Rope Progenitor and Driver of a Large-Scale CME and Wave. *Solar Phys.* 291, 1173–1208.
- Grechnev, V. V., Uralov, A. M., Kuzmenko, I. V., Kochanov, A. A., Chertok, I. M., Kalashnikov, S. S., 2015. Responsibility of a Filament Eruption for the Initiation of a Flare, CME, and Blast Wave, and its Possible Transformation into a Bow Shock. *Solar Phys.* 290, 129–158.
- Grechnev, V. V., Uralov, A. M., Slemzin, V. A., Chertok, I. M., Filippov, B. P., Rudenko, G. V., Temmer, M., 2014b. A Challenging Solar Eruptive Event of 18 November 2003 and the Causes of the 20 November Geomagnetic Superstorm. I. Unusual History of an Eruptive Filament. *Solar Phys.* 289, 289–318.
- Grechnev, V. V., Uralov, A. M., Slemzin, V. A., Chertok, I. M., Kuzmenko, I. V., Shibasaki, K., 2008. Absorption Phenomena and a Probable Blast Wave in the 13 July 2004 Eruptive Event. *Solar Phys.* 253, 263–290.
- Grechnev, V. V., Uralov, A. M., Zandanov, V. G., Rudenko, G. V., Borovik, V. N., Grigorjeva, I. Y., Slemzin, V. A., Bogachev, S. A., Kuzin, S. V., Zhitnik, I., Pertsov, A. A., Shibasaki, K., Livshits, M. A., 2006. Plasma Parameters in a Post-Eruptive Arcade Observed with CORONAS-F/SPIRIT, Yohkoh/SXT, SOHO/EIT, and in Microwaves. *Publ. Astron. Soc. Japan* 58, 55–68.
- Hirayama, T., 1974. Theoretical Model of Flares and Prominences. I: Evaporating Flare Model. *Solar Phys.* 34, 323–338.
- Hudson, H. S., Khan, J. I., Lemen, J. R., Nitta, N. V., Uchida, Y., 2003. Soft X-ray observation of a large-scale coronal wave and its exciter. *Solar Phys.* 212, 121–149.
- Inhester, B., Birn, J., Hesse, M., 1992. The evolution of line-tied coronal arcades including a converging footpoint motion. *Solar Phys.* 138, 257–281.
- Kahler, S. W., Sheeley, Jr., N. R., Liggett, M., 1989. Coronal mass ejections and associated X-ray flare durations. *Astrophys. J.* 344, 1026–1033.
- Knock, S. A., Cairns, I. H., 2005. Type II radio emission predictions: Sources of coronal and interplanetary spectral structure. *J. Geophys. Res. (Space Physics)* 110, A01101.
- Kochanov, A. A., Anfinogentov, S. A., Prosovetsky, D. V., Rudenko, G. V., Grechnev, V. V., 2013. Imaging of the Solar Atmosphere by the Siberian Solar Radio Telescope at 5.7 GHz with an Enhanced Dynamic Range. *Publ. Astron. Soc. Japan* 65, S19.
- Kuzmenko, I. V., Grechnev, V. V., 2017. Development and Parameters of a Non-Self-Similar CME Caused by the Eruption of a Quiescent Prominence. *Solar Phys.* 292, 143.
- Kuzmenko, I. V., Grechnev, V. V., Uralov, A. M., 2009. A study of eruptive solar events with negative radio bursts. *Astron. Rep.* 53, 1039–1049.
- Kuzmenko, I. V., Mikhailina, F. A., Kapustin, B. A., 2008. RT-2 radio telescope of the Ussuriysk Astrophysical Observatory: current state and observation data. *Radiophysics and Quantum Electronics* 51, 905–909.
- Kwon, R.-Y., Zhang, J., Olmedo, O., 2014. New Insights into the Physical Nature of Coronal Mass Ejections and Associated Shock Waves within the Framework of the Three-dimensional Structure. *Astrophys. J.* 794, 148.
- Kwon, R.-Y., Zhang, J., Vourlidis, A., 2015. Are Halo-like Solar Coronal Mass Ejections Merely a Matter of Geometric Projection Effects? *Astrophys. J. Lett.* 799, L29.
- Lemen, J. R., Title, A. M., Akin, D. J., Boerner, P. F., Chou, C., Drake, J. F., Duncan, D. W., Edwards, C. G., Friedlaender, F. M., Heyman, G. F., Hurlburt, N. E., Katz, N. L., Kushner, G. D., Levay, M., Lindgren, R. W., Mathur, D. P., McFeaters, E. L., Mitchell, S., Rehse, R. A., Schrijver, C. J., Springer, L. A., Stern, R. A., Tarbell, T. D., Wuelser, J.-P., Wolfson, C. J., Yanari, C., Bookbinder, J. A., Cheimets, P. N., Caldwell, D., Deluca, E. E., Gates, R., Golub, L., Park, S., Podgorski, W. A., Bush, R. I., Scherrer, P. H., Gummin, M. A., Smith, P., Aufer, G., Jerram, P., Pool, P., Soufli, R., Windt, D. L., Beardsley, S., Clapp, M., Lang, J., Waltham, N., 2012. The Atmospheric Imaging Assembly (AIA) on the Solar Dynamics Observatory (SDO). *Solar Phys.* 275, 17–40.
- Lesovoi, S., Altyntsev, A., Kochanov, A., Grechnev, V., Gubin, A., Zhdanov, D., Ivanov, E., Uralov, A., Kashapova, L., Kuznetsov, A., Meshalkina, N., Sych, R., 2017. Siberian Radioheliograph: first results. *Solar-Terrestrial Physics* 3 (1), 3–18.
- Lesovoi, S., Kobets, V., 2017. Correlation plots of the Siberian Radioheliograph. *Solar-Terrestrial Physics* 3 (1), 19–25.
- Lesovoi, S. V., Altyntsev, A. T., Ivanov, E. F., Gubin, A. V., 2014. A 96-antenna radioheliograph. *Research in Astronomy and Astrophysics* 14, 864–868.
- Lin, R. P., Dennis, B. R., Hurford, G. J., Smith, D. M., Zehnder, A., Harvey, P. R., Curtis, D. W., Pankow, D., Turin, P., Bester, M., Csillaghy, A., Lewis, M., Madden, N., van Beek, H. F., Appleby, M., Raudorf, T., McTiernan, J., Ramaty, R., Schmahl, E., Schwartz, R., Krucker, S., Abiad, R., Quinn, T., Berg, P., Hashii, M., Sterling, R., Jackson, R., Pratt, R., Campbell, R. D., Malone, D., Landis, D., Barrington-Leigh, C. P., Slassi-Sennou, S., Cork, C., Clark, D., Amato, D., Orwig, L., Boyle, R., Banks, I. S., Shirey, K., Tolbert, A. K., Zarro, D., Snow, F., Thomsen, K., Henneck, R., McHedlishvili, A., Ming, P., Fivian, M., Jordan, J., Wanner, R., Crubb, J., Preble, J., Mantranga, M., Benz, A., Hudson, H., Canfield, R. C., Holman, G. D., Cranell, C., Kosugi, T., Emslie, A. G., Vilmer, N., Brown, J. C., Johns-Krull, C., Aschwanden, M., Metcalf, T., Conway, A., 2002. The Reuven Ramaty

- High-Energy Solar Spectroscopic Imager (RHESSI). *Solar Phys.* 210, 3–32.
- Long, D. M., Murphy, P., Graham, G., Carley, E. P., Pérez-Suárez, D., 2017. A Statistical Analysis of the Solar Phenomena Associated with Global EUV Waves. *Solar Phys.* 292, 185.
- Longcope, D. W., Beveridge, C., 2007. A Quantitative, Topological Model of Reconnection and Flux Rope Formation in a Two-Ribbon Flare. *Astrophys. J.* 669, 621–635.
- Low, B. C., 1982. Self-similar magnetohydrodynamics. I - The  $\gamma = 4/3$  polytrope and the coronal transient. *Astrophys. J.* 254, 796–805.
- Lv, M. S., Chen, Y., Li, C. Y., Zimovets, I., Du, G. H., Wang, B., Feng, S. W., Ma, S. L., 2017. Sources of the Multi-Lane Type II Solar Radio Burst on 5 November 2014. *Solar Phys.* 292, 194.
- Magdalenic, J., Marqué, C., Zhukov, A. N., Vršnak, B., Žic, T., 2010. Origin of Coronal Shock Waves Associated with Slow Coronal Mass Ejections. *Astrophys. J.* 718, 266–278.
- Magdalenic, J., Marqué, C., Zhukov, A. N., Vršnak, B., Veronig, A., 2012. Flare-generated Type II Burst without Associated Coronal Mass Ejection. *Astrophys. J.* 746, 152.
- Maksimov, V. P., Nefed'ev, V. P., 1991. The observation of a 'negative burst' with high spatial resolution. *Solar Phys.* 136, 335–342.
- Mann, G., Klassen, A., Aurass, H., Klassen, H.-T., 2003. Formation and development of shock waves in the solar corona and the near-Sun interplanetary space. *Astron. Astrophys.* 400, 329–336.
- Masson, S., Pariat, E., Aulanier, G., Schrijver, C. J., 2009. The Nature of Flare Ribbons in Coronal Null-Point Topology. *Astrophys. J.* 700, 559–578.
- Meegan, C., Lichti, G., Bhat, P. N., Bissaldi, E., Briggs, M. S., Connaughton, V., Diehl, R., Fishman, G., Greiner, J., Hoover, A. S., van der Horst, A. J., von Kienlin, A., Kippen, R. M., Kouveliotou, C., McBreen, S., Paciesas, W. S., Preece, R., Steinle, H., Wallace, M. S., Wilson, R. B., Wilson-Hodge, C., 2009. The Fermi Gamma-ray Burst Monitor. *Astrophys. J.* 702, 791–804.
- Meshalkina, N. S., Uralov, A. M., Grechnev, V. V., Altyntsev, A. T., Kashapova, L. K., 2009. Eruptions of Magnetic Ropes in Two Homologous Solar Events of 2002 June 1 and 2: a Key to Understanding an Enigmatic Flare. *Publ. Astron. Soc. Japan* 61, 791–803.
- Miklenic, C. H., Veronig, A. M., Vršnak, B., 2009. Temporal comparison of nonthermal flare emission and magnetic-flux change rates. *Astron. Astrophys.* 499, 893–904.
- Muhr, N., Veronig, A. M., Kienreich, I. W., Temmer, M., Vršnak, B., 2011. Analysis of Characteristic Parameters of Large-scale Coronal Waves Observed by the Solar-Terrestrial Relations Observatory/Extreme Ultraviolet Imager. *Astrophys. J.* 739, 89.
- Muhr, N., Veronig, A. M., Kienreich, I. W., Vršnak, B., Temmer, M., Bein, B. M., 2014. Statistical Analysis of Large-Scale EUV Waves Observed by STEREO/EUVI. *Solar Phys.* 289, 4563–4588.
- Nakajima, H., Nishio, M., Enome, S., Shibasaki, K., Takano, T., Hanaoka, Y., Torii, C., Sekiguchi, H., Bushimata, T., Kawashima, S., Shinohara, N., Irimajiri, Y., Koshiishi, H., Kosugi, T., Shiomi, Y., Sawa, M., Kai, K., 1994. The Nobeyama radioheliograph. *IEEE Proceedings* 82, 705–713.
- Nakajima, H., Sekiguchi, H., Sawa, M., Kai, K., Kawashima, S., 1985. The radiometer and polarimeters at 80, 35, and 17 GHz for solar observations at Nobeyama. *Publ. Astron. Soc. Japan* 37, 163–170.
- Neupert, W. M., 1968. Comparison of Solar X-Ray Line Emission with Microwave Emission during Flares. *Astrophys. J. Lett.* 153, L59.
- Ninos, A., Alissandrakis, C. E., Hillaris, A., Preka-Papadema, P., 2011. On the relationship of shock waves to flares and coronal mass ejections. *Astron. Astrophys.* 531, A31.
- Nitta, N. V., Aschwanden, M. J., Boerner, P. F., Freeland, S. L., Lemen, J. R., Wuelser, J.-P., 2013a. Soft X-ray Fluxes of Major Flares Far Behind the Limb as Estimated Using STEREO EUV Images. *Solar Phys.* 288, 241–254.
- Nitta, N. V., Hudson, H. S., 2001. Recurrent flare/CME events from an emerging flux region. *Geophys. Res. Lett.* 28, 3801–3804.
- Nitta, N. V., Liu, W., Gopalswamy, N., Yashiro, S., 2014. The Relation Between Large-Scale Coronal Propagating Fronts and Type II Radio Bursts. *Solar Phys.* 289, 4589–4606.
- Nitta, N. V., Schrijver, C. J., Title, A. M., Liu, W., 2013b. Large-scale Coronal Propagating Fronts in Solar Eruptions as Observed by the Atmospheric Imaging Assembly on Board the Solar Dynamics Observatory—An Ensemble Study. *Astrophys. J.* 776, 58.
- Qiu, J., Hu, Q., Howard, T. A., Yurchyshyn, V. B., 2007. On the Magnetic Flux Budget in Low-Corona Magnetic Reconnection and Interplanetary Coronal Mass Ejections. *Astrophys. J.* 659, 758–772.
- Reiner, M. J., Vourlidas, A., Cyr, O. C. S., Burckpile, J. T., Howard, R. A., Kaiser, M. L., Prestage, N. P., Bougeret, J.-L., 2003. Constraints on Coronal Mass Ejection Dynamics from Simultaneous Radio and White-Light Observations. *Astrophys. J.* 590, 533–546.
- Rouillard, A. P., Plotnikov, I., Pinto, R. F., Tirole, M., Lavarra, M., Zucca, P., Vainio, R., Tylka, A. J., Vourlidas, A., De Rosa, M. L., Linker, J., Warmuth, A., Mann, G., Cohen, C. M. S., Mewaldt, R. A., 2016. Deriving the Properties of Coronal Pressure Fronts in 3D: Application to the 2012 May 17 Ground Level Enhancement. *Astrophys. J.* 833, 45.
- Saito, K., 1970. A non-spherical axisymmetric model of the solar K corona of the minimum type. *Annals of the Tokyo Astronomical Observatory* 12, 53–120.
- Sawyer, C., 1977. Are 'negative bursts' due to absorption. *Solar Phys.* 51, 203–215.
- Scherrer, P. H., Schou, J., Bush, R. I., Kosovichev, A. G., Bogart, R. S., Hoeksema, J. T., Liu, Y., Duvall, T. L., Zhao, J., Title, A. M., Schrijver, C. J., Tarbell, T. D., Tomczyk, S., 2012. The Helioseismic and Magnetic Imager (HMI) Investigation for the Solar Dynamics Observatory (SDO). *Solar Phys.* 275, 207–227.
- Shanmugaraju, A., Moon, Y.-J., Cho, K.-S., Dryer, M., Umapathy, S., 2006. Origin of Coronal Shocks without Mass Ejections. *Solar Phys.* 233, 117–127.
- Sheeley, N. R., Wang, Y.-M., Hawley, S. H., Brueckner, G. E., Dere, K. P., Howard, R. A., Koomen, M. J., Korendyke, C. M., Michels, D. J., Paswaters, S. E., Socker, D. G., St. Cyr, O. C., Wang, D., Lamy, P. L., Llebaria, A., Schwenn, R., Simnett, G. M., Plunkett, S., Biesecker, D. A., 1997. Measurements of Flow Speeds in the Corona Between 2 and 30  $R_{sun}$ . *Astrophys. J.* 484, 472–478.
- Sheeley, Jr., N. R., Warren, H. P., Wang, Y.-M., 2007. A Streamer Ejection with Reconnection Close to the Sun. *Astrophys. J.* 671, 926–935.
- Smolkov, G. I., Pistolkors, A. A., Treskov, T. A., Krissinel, B. B., Putilov, V. A., 1986. The Siberian solar radio-telescope - Parameters and principle of operation, objectives and results of first observations of spatio-temporal properties of development of active regions and flares. *Astrophys. Spa. Sci.* 119, 1–4.
- Temmer, M., Rollett, T., Möstl, C., Veronig, A. M., Vršnak, B., Odstrčil, D., 2011. Influence of the Ambient Solar Wind Flow on the Propagation Behavior of Interplanetary Coronal Mass Ejections. *Astrophys. J.* 743, 101.
- Temmer, M., Veronig, A. M., Vršnak, B., Rybák, J., Gömöry, P., Stoiser, S., Maričić, D., 2008. Acceleration in Fast Halo CMEs and Synchronized Flare HXR Bursts. *Astrophys. J. Lett.* 673, L95.
- Thalmann, J. K., Su, Y., Temmer, M., Veronig, A. M., 2015. The Confined X-class Flares of Solar Active Region 2192. *Astrophys. J. Lett.* 801, L23.
- Torii, C., Tsukiji, Y., Kobayashi, S., Yoshimi, N., Tanaka, H., Enome, S., 1979. Full-automatic radiopolarimeters for solar patrol at microwave frequencies. Nagoya University, Research Institute of Atmospheric, Proceedings 26, 129–132.
- Uralov, A. M., Grechnev, V. V., Hudson, H. S., 2005. Initial localization and kinematic characteristics of the structural components of a coronal mass ejection. *J. Geophys. Res. (Space Physics)* 110, A05104.
- Uralov, A. M., Grechnev, V. V., Rudenko, G. V., Myshyakov, I. I., Chertok, I. M., Filippov, B. P., Slemzin, V. A., 2014. A Challenging Solar Eruptive Event of 18 November 2003 and the Causes of the 20 November Geomagnetic Superstorm. III. Catastrophe of the Eruptive Filament at a Magnetic Null Point and Formation of an Opposite-Handedness CME. *Solar Phys.* 289, 3747–3772.
- Uralova, S. V., Uralov, A. M., 1994. WKB approach to the problem of MHD shock propagation through the heliospheric current sheet. *Solar Phys.* 152, 457–479.
- Veronig, A. M., Temmer, M., Vršnak, B., 2008. High-Cadence Observations of a Global Coronal Wave by STEREO EUVI. *Astrophys. J. Lett.* 681, L113.
- Vršnak, B., 2006. Forces governing coronal mass ejections. *Adv. Space Res.* 38, 431–440.
- Vršnak, B., 2008. Processes and mechanisms governing the initiation and propagation of CMEs. *Annales Geophysicae* 26, 3089–3101.
- Vršnak, B., Cliver, E. W., 2008. Origin of Coronal Shock Waves. *Invited Review. Solar Phys.* 253, 215–235.
- Vršnak, B., Gopalswamy, N., 2002. Influence of the aerodynamic drag on the motion of interplanetary ejecta. *J. Geophys. Res. (Space Physics)* 107, 1019.
- Wang, Y., Zhang, J., Shen, C., 2009. An analytical model probing the internal

- state of coronal mass ejections based on observations of their expansions and propagations. *J. Geophys. Res. (Space Physics)* 114 (A13), A10104.
- Warmuth, A., 2015. Large-scale Globally Propagating Coronal Waves. *Living Reviews in Solar Physics* 12, 3.
- Warmuth, A., Mann, G., Aurass, H., 2005. First Soft X-Ray Observations of Global Coronal Waves with the GOES Solar X-Ray Imager. *Astrophys. J. Lett.* 626, L121–L124.
- Warmuth, A., Vršnak, B., Aurass, H., Hanslmeier, A., 2001. Evolution of Two EIT/H $\alpha$  Moreton Waves. *Astrophys. J. Lett.* 560, L105–L109.
- Warmuth, A., Vršnak, B., Magdalenic, J., Hanslmeier, A., Otruba, W., 2004a. A multiwavelength study of solar flare waves. I. Observations and basic properties. *Astron. Astrophys.* 418, 1101–1115.
- Warmuth, A., Vršnak, B., Magdalenic, J., Hanslmeier, A., Otruba, W., 2004b. A multiwavelength study of solar flare waves. II. Perturbation characteristics and physical interpretation. *Astron. Astrophys.* 418, 1117–1129.
- Yashiro, S., Gopalswamy, N., Michalek, G., St. Cyr, O. C., Plunkett, S. P., Rich, N. B., Howard, R. A., 2004. A catalog of white light coronal mass ejections observed by the SOHO spacecraft. *J. Geophys. Res. (Space Physics)* 109, A07105.
- Zhang, J., Dere, K. P., Howard, R. A., Kundu, M. R., White, S. M., 2001. On the Temporal Relationship between Coronal Mass Ejections and Flares. *Astrophys. J.* 559, 452–462.
- Zhdanov, D. A., Zandanov, V. G., 2015. Observations of Microwave Fine Structures by the Badary Broadband Microwave Spectropolarimeter and the Siberian Solar Radio Telescope. *Solar Phys.* 290, 287–294.
- Zhukov, A. N., Auchère, F., 2004. On the nature of EIT waves, EUV dimmings and their link to CMEs. *Astron. Astrophys.* 427, 705–716.
- Zirin, H., Baumert, B. M., Hurford, G. J., 1991. The microwave brightness temperature spectrum of the quiet sun. *Astrophys. J.* 370, 779–783.